Article:
Gomez Martin, JC, Bones, DL, Carrillo Sánchez, JD et al. (2017) Novel Experimental Simulations of the Atmospheric Injection of Meteoric Metals. The Astrophysical Journal, 83 (2). 212. ISSN: 0004-637X

https://doi.org/10.3847/1538-4357/aa5c8f

Novel Experimental Simulations of the Atmospheric Injection of Meteoric Metals

J. C. Gómez Martín[1], D. L. Bones[1], J. D. Carrillo-Sánchez[1], A. D. James[1], J. M. Trigo-Rodríguez[2], B. Fegley Jr.[3] and J.M.C. Plane[1]*

1 School of Chemistry, University of Leeds, Woodhouse Lane, LS2 9JT, Leeds, UK

2 Meteorites, Minor Bodies and Planetary Science Group, Institute of Space Sciences (CSIC-IEEC). Campus UAB, C/ Can Magrans s/n, 08193 Cerdanyola del Vallés (Barcelona), Spain

3 Washington University, St. Louis, MO, USA

*Correspondence to: J.M.C.Plane@leeds.ac.uk

Abstract

A newly-developed laboratory Meteor Ablation Simulator (MASI) is used to test model predictions of the atmospheric ablation of interplanetary dust particles (IDPs) with experimental Na, Fe and Ca vaporisation profiles. MASI is the first laboratory set-up capable of performing time-resolved atmospheric ablation simulations, by means of precision resistive heating and atomic laser induced fluorescence detection. Experiments using meteoritic IDP analogues show that at least three mineral phases (Na-rich plagioclase, metal-sulfide and Mg-rich silicate) are required to explain the observed appearance temperatures of the vaporized elements. Low melting temperatures of Na-rich plagioclase and metal-sulfide, compared to silicate grains, preclude equilibration of all the elemental constituents in a single melt. The phase change process of distinct mineral components determines the way in which Na and Fe evaporate. Ca evaporation is dependent on particle size and on the initial composition of the molten silicate.

Measured vaporized fractions of Na, Fe and Ca as a function of particle size and speed confirm differential ablation (i.e. the most volatile elements such as Na ablate first, followed by the main constituents Fe, Mg and Si, and finally the most refractory elements such as Ca). The Chemical Ablation Model (CABMOD) (Vondrak et al. 2008) provides a reasonable approximation to this effect based on chemical fractionation of a molten silicate in thermodynamic equilibrium, even though the compositional and geometric description of IDPs is simplistic. Improvements in the model are required in order to better reproduce the specific shape of the elemental ablation profiles.

1. Introduction

The inner solar system is full of dust particles originating from cometary trails and collisions between asteroids (Ceplecha et al. 1998). As a consequence, tonnes of submillimetre meteoroids, which we term interplanetary dust particles (IDP)[1], enter the Earth's atmosphere every day. This extra-terrestrial input has a wide range of impacts including the formation of layers of metal atoms and ions in the mesosphere and lower thermosphere, the nucleation of noctilucent clouds, removal of stratospheric sulfuric acid, chemical interactions with stratospheric aerosol, and the deposition of bioavailable Fe (Plane, Feng, & Dawkins 2015). As a result of their high atmospheric entry velocities, IDPs experience rapid frictional heating with air molecules, which can cause them to melt and rapidly vaporise forming a meteor. Meteoric ablation is the process by which the elemental constituents (O, Si, Fe, Mg, Ni, Na, Ca, Al, etc.) of an IDP captured by the gravity of a planet are released in the atmosphere due to: i) sputtering by collisions with atmospheric molecules and ii) thermal evaporation. This process occurs on Earth between80 and 120 km (Vondrak, et al. 2008). Sometimes fragmentation of the incoming particles into smaller pieces and sweeping of liquid films is also referred to as meteoric ablation. These processes are highly uncertain for the range of submillimetre particles that dominate the extra-terrestrial mass flux, and so are not considered in the present work.

Initially, the relative meteoric metal injection rates arising from meteoric ablation were assumed to correspond to meteoritic abundances (Plane 1991), close to CI or CM (Taylor, Matrajt, & Guan 2012). However chemical ablation models (McNeil, Murad, &

[1] Historically, the term IDP has been reserved for the subset of Zodiacal Cloud particles that are captured by Earth's gravity and reach the Earth's stratosphere relatively intact. We find this definition too narrow. On the other hand, the term cosmic dust seems too general to refer to interplanetary dust. Therefore we prefer using IDP to define the cosmic dust particles that form the Zodiacal Cloud. IDPs collected in the stratosphere will be referred to here as S-IDPs.

Plane 2002; Vondrak, et al. 2008) based on thermodynamic melt models such as MAGMA (Schaefer & Fegley Jr 2004a) and laboratory experiments (Hashimoto 1983; Notsu et al. 1978) indicated that fractionation involving early evaporation of volatile elements (K and Na), termed differential ablation, should occur, which was subsequently observed using a high performance radar (Janches et al. 2009). Differential ablation has also been seen by optical spectroscopic observations of fireballs formed by much larger particles (Borovicka 1993). The CI chondritic abundance of Na relative to Fe is 1:15, while the Na ablation rate relative to Fe is required to be ~1:4 in atmospheric models (Carrillo-Sánchez et al. 2015). Even more extreme is the case of Ca, which is in a CI ratio of 1:1 to Na, but is depleted by a factor of ~40 in the mesosphere. Fireball spectra also show relative abundances of Ca relative to Fe much lower than chondritic, indicating that Ca-phases escape complete evaporation (Trigo-Rodriguez et al. 2003). Consistent with atmospheric observations, volatile elements (Na, S) are depleted in micrometeorites (MMs) (Jessberger et al. 2001). Moreover, mass-dependent isotopic fractionation of volatile elements (K, O) has been observed in certain MMs, implying different degrees of loss to the atmosphere (Taylor et al. 2005).

Atoms released during ablation are ionised by hyperthermal collisions with atmospheric molecules, which results in an envelope of free electrons around the meteor that backscatters radar waves, enabling detection of the so-called head echo (Janches et al. 2006). Evaporation of Na is then important for radar detection of small/slow meteoroids which marginally ablate, due to higher volatility and its low ionisation potential. The fate of the evaporated metals is reaction with atmospheric constituents, eventually re-condensing in the form of Meteor Smoke Particles (MSPs), through which the meteoric input has its most important impacts in the atmosphere. The unablated fraction of IDPs constitutes the flux of unmelted and scoriaceous MMs and cosmic spherules to the surface, which have been

collected in sea sediments, deserts and the polar caps (Brownlee 2016; Taylor, Messenger, & Folco 2016).

The Chemical Ablation Model (CABMOD) (Vondrak, et al. 2008) estimates the ablation rate profiles of individual elements for a meteoroid with specified composition, mass, velocity, and entry angle. This model has therefore been at the core of recent efforts to quantify the input of IDPs into the terrestrial atmosphere by reconciling observations ranging from MM samples collected at the surface to astronomical observations of the Zodiacal infrared emission (Carrillo-Sánchez, et al. 2015; Plane 2012). CABMOD has been used previously in combination with mass and velocity distribution of IDPs derived from different observations in order to explain atmospheric metal relative abundances and the flux of micrometeorites and spherules collected in the polar icecaps (Carrillo-Sánchez, et al. 2015). The mass and velocity distribution of IDPs derived from High Performance Large Aperture (HPLA) radar observations at Arecibo (Janches, et al. 2006) are very different from those inferred from orbital impact detection by the Long Duration Exposure Facility (LDEF) (Love & Brownlee 1993) and Infrared Astronomical Satellite (IRAS) observations of the Zodiacal Cloud (Nesvorný et al. 2010), which leads to disparate fluxes of gas-phase meteoric metals and MMs (Carrillo-Sánchez, et al. 2015; Plane 2012). This difference has been interpreted as a result of the bias of radars towards fast/large meteoroids (Janches et al. 2014; Janches et al. 2015). The best match of metal layer density ratios and the fluxes of MMs and spherules is obtained when CABMOD is combined with an astronomical dust model constrained by Zodiacal Cloud observations, although some discrepancies between model and observations persist (Carrillo-Sánchez, et al. 2015).

In order to reduce uncertainties in ablation modelling it is clearly necessary to set CABMOD on solid experimental ground. There have not been many attempts to simulate

micrometeoroid ablation in laboratory experiments. Most previous studies performing experimental simulations of the atmospheric entry of IDPs have focussed on understanding the thermal processing of MMs retrieved on the ground both from a textural and compositional perspective, in order to infer their origin (Greshake et al. 1998; Sandford & Bradley 1989; Toppani et al. 2001). Evaporation experiments in a vacuum have been conducted in the past in order to understand chemical fractionation in synthetic CI melts (Hashimoto 1983). More recent experiments using pyrolysis and gas phase Infrared Spectroscopy have also attempted to quantify the yield of SO_2, CO_2 and H_2O in order to estimate the potential impact of micrometeoroids on planetary atmospheres (Court & Sephton 2009, 2011).

CABMOD includes a standard treatment of meteor physics: the balance of momentum lost by the incoming meteor by momentum gained by impinging atmospheric molecules, as well as the balance of frictional heating by radiative loss, absorption of heat energy through temperature increase and phase transitions (Love & Brownlee 1991). Melting occurs if the temperature exceeds the melting point of the meteoroid. Langmuir evaporation into a vacuum is assumed (Love & Brownlee 1991), where the evaporative loss rate of a species *i* from the melt is given by the Hertz-Knudsen expression:

$$\frac{dm_i}{dt} = f(T)\gamma_i p_i S \sqrt{\frac{M_i}{2\pi k_B T}} \quad \text{(E1)}$$

S is the surface area of the particle, M_i is the molecular weight of the species *i*, k_B the Boltzmann's constant, *T* the temperature, p_i the gas-liquid equilibrium vapour pressure, γ_i the apparent evaporation coefficient and $f(T)$ the phase transition factor. Vapour pressures are calculated from the multicomponent gas-melt chemical equilibrium code MAGMA (Fegley & Cameron 1987; Schaefer & Fegley Jr 2004a). MAGMA was validated by (Schaefer & Fegley Jr 2004b) by successful modelling of the residual compositions resulting from

experiments of partial evaporation into a vacuum of synthetic CI-like and CAIs-like materials[2] (Hashimoto 1983; Wang et al. 2001) and of lunar aluminiferous basalt (Markova et al. 1986) (Richter et al. 2002). A potential problem is that much of the thermodynamic data in MAGMA has to be extrapolated to $T > 2000$ K from measurements below 1700 K. Thermodynamic properties of silicate melts have not been measured at $T > 2000$ K in most cases, and thus the Gibbs free energies of the relevant phase change reactions (equivalently the equilibrium constants between the melt and vapour phases) are extrapolated above 2000 K from data measured at lower temperatures. In CABMOD, the apparent evaporation coefficient γ_i (also referred to as sticking or uptake coefficient) is assumed to be unity for all species. Here, a possible shortcoming is that γ_i, which is 1 for pure metals (Safarian & Engh 2012), may be lower than 1 in silicate melts (Alexander 2002), because diffusion from the bulk into the surface film may become rate-limiting. In CABMOD the phase transition (the temperature range where the solid and the liquid are in equilibrium) is treated by applying a sigmoid temperature dependence weighting $f(T)$ between 0 and 1 to the equilibrium vapour pressure:

$$f(T) = (1 + \exp(-(T - T_c)/\tau)^{-1} \quad \text{(E2)}$$

where τ is a constant that characterises the width of the sigmoid profile and T_c the temperature such that $f(T_c) = 0.5$. The values $T_c = 1800$ K and $\tau = 14$ K are prescribed by the olivine Fa_{50} solid-liquid equilibrium temperature range, meaning essentially that $f(T < 1700$ K$)=0$ and $f(T > 1800$ K$) = 1$ (Vondrak, et al. 2008).

An important assumption in CABMOD is the mineralogy of IDPs. The current view is that IDPs are of mainly of cometary origin and related to carbonaceous chondrites (Noguchi et al. 2015; Taylor, et al. 2012), in contrast to terrestrial meteorites, most of which are

[2] CAIs: calcium- aluminium-rich inclusions

ordinary chondrites. About 75% of IDPs are estimated to be CI and CM-like fine-grained aggregates containing a variety of anhydrous and hydrated silicate minerals (Taylor, et al. 2012) as well as troilite (FeS) and Fe-Ni alloy. Hydrated silicates undergo chemical and mineralogical reactions above 900 K (Greshake, et al. 1998) and the melting points of anhydrous minerals span a range of temperature between ~1400 and 2200 K. The technical challenge of modelling melting and evaporation of multiphase aggregate particles have imposed the current working assumption in CABMOD of single mineral IDPs. Such a single mineral composition is an idealization, since no single phase has CI composition for all the elemental constituents. Because olivine is a major constituent (Jessberger, et al. 2001) or precursor (Greshake, et al. 1998; Sandford & Bradley 1989) of MMs and S-IDPs, and because the MgO, FeO and SiO_2 abundances in CI chondrites are very close to the Mg_2SiO_4-Fe_2SiO_4 pseudo-binary join in the MgO-FeO-SiO_2 ternary phase diagram (Hashimoto 1983; Wu et al. 1993), it has been assumed that IDPs melt following the binary phase diagram of olivine.

The first objective of this study is refining and validating CABMOD using a laboratory experimental set-up which, for the first time, enables time-resolved simulations of the melting of IDPs analogues and the subsequent evaporation of their major elemental constituents under conditions of atmospheric entry. Specifically, the assumptions of monolithic IDPs with a single mineral composition and of Langmuir evaporation need to be tested. The second, related, objective is to test the CABMOD prediction of differential ablation of Fe and Ca with respect to Na.

2. Experimental methods

The Meteoric Ablation Simulator (MASI) has been designed to carry out controlled flash heating of IDP analogues over the range of atmospheric ablation temperatures, while the

vaporisation rates of two elemental constituents are monitored using time-resolved atomic laser induced fluorescence (LIF). A detailed description and characterisation of the apparatus is reported by Bones et al. (2016). The MASI consists of a vacuum chamber fitted with an electrical feed-through on which a 20 mm long and 1 mm wide tungsten ribbon is mounted as a filament (Fig. 1). Samples of IDP analogues are deposited on the filament surface and then the chamber is closed and evacuated. A flow of 5 standard cubic centimetres per minute (sccm) of oxygen-free N_2 (OFN N_2 BOC 99.998%) is passed through the chamber. This maintains a background pressure of ~15 Pa, high enough to slow down diffusion towards the walls, but still low enough to allow the assumption of evaporation into a vacuum (the mean free path is ~1 mm, much larger than the dimensions of the particles). The upper limit O_2 fugacity under these conditions is $\log fO_2 < -9.4$, and therefore the experiments are carried out under reducing conditions (Toppani & Libourel 2003). The filament is resistively heated using a programmable power supply up to 3000 K. The temperature of the filament surface is measured using a 15 ms time response pyrometer camera (Land Ametek System 4), whose factory calibration settings were checked by observing the melting temperature of a Fe wire. Each experiment is recorded through a set of optics and filters using a video camera in order to track the particle evolution on the surface of the filament.

The doubled and tripled outputs from a Nd:YAG laser (Litron Nano) operating at 250 Hz are used to pump two dye lasers (Sirah Cobra) tuned to the atomic Na and Fe (or Ca) resonance transitions at 588.99 nm and 248.33 nm (or 422.67 nm), respectively. The laser beams pass 3.5 cm above the filament and promote evaporated atoms to an excited state. The photons emitted by radiative relaxation to the ground state (fluorescence) are collected through monochromators (Mini-chrom Optometrics) by orthogonal photomultipliers (THORN EMI 9861QB) connected to boxcar averagers. The LIF signal at the detection volume is proportional to the concentration of atoms in the gas envelope evaporated from the

particle according to the solution of the diffusion equation in spherical symmetry (for a region bounded internally by a sphere (Crank 1975). The concentration in the particle gas phase envelope is proportional to the particle mass loss rate given by the Hertz-Knudsen expression (E1), because the mass loss rate varies over a time scale of tenths of a second, much longer than the time scale of a LIF measurement (boxcar gate width ~100 ns).

A microcomputer-controlled delay generator (National Instruments Compact-RIO) is used to synchronise the laser firing with temperature ramping and LIF signal acquisition. In a typical experiment a heating program is run and the LIF signals of the evaporated metals are recorded together with the observed temperature and the time. Different heating programs can be chosen, including ramps of different slopes, step functions, and modelled atmospheric entry temperature profiles calculated from the momentum and energy balance equations (Vondrak, et al. 2008). A linear ramp is a convenient choice for carrying out model benchmarking experiments, since it allows a straightforward conversion of the time abscissa into temperature, thus allowing an easy visualization of the signal appearance temperature. Linear ramps also enable complete evaporation of the more refractory elemental constituents (in this study Fe and Ca), because high enough temperatures can be maintained for a few seconds. Linear heating ramps were therefore used to test evaporation kinetics, thermodynamic, compositional and structural assumptions in CABMOD, prior to the simulations of atmospheric ablation. Since heat is not supplied by air friction as in atmospheric entry but by conduction, MASI can only simulate the thermal ablation (evaporation) of the elemental constituents of IDPs. Previous work with CABMOD (Vondrak, et al. 2008) has shown that non-thermal losses (sputtering) are very minor for the bulk of the incoming flux of IDPs. To avoid confusion, the term evaporation will be used throughout this paper to refer to the loss of elemental constituents from IDP analogues in MASI experiments, while ablation will be reserved to the loss of elemental constituents from

sub-millimetre IDPs upon atmospheric entry (even though this is mainly due to evaporation). Physical disintegration of particles by fragmentation or sweeping of liquid films are highly uncertain for submillimetre particles.

The selection of representative IDP analogues is an important aspect of these experiments. Unmelted IDPs (R > 50 μm) collected in different studies consist of fine-grained aggregates and are similar to the matrix of carbonaceous chondrites, with a minor population of ordinary chondritic aggregates and anhydrous minerals (Dobrică et al. 2009; Taylor, et al. 2012). Carbonaceous porous S-IDPs and MMs with R < 50 μm have also been retrieved (Noguchi, et al. 2015; Zolensky & Lindstrom 1992). In order to account for some of the properties of these populations, samples of the Allende (Krinov 1970) (CV3), Murchison (Fuchs, Olsen, & Jensen 1973) (CM2) and Chergach (Weisberg et al. 2008) (H5) meteorites, and of terrestrial Mg-rich olivine and Na-rich and Ca-rich plagioclases were used in the MASI experiments (Table 1). The IDP analogues are prepared by grinding pieces of each meteorite/mineral and separating them using mechanical dry sieving into six size classes or bins with radii <19, 19-43, 53-75, 75-125, 125-177, >177 μm (Fig. 2, panel *a*), encompassing the IDP size range (R < 200 μm) that makes the largest contribution to the atmospheric input (Love & Brownlee 1993; Nesvorný et al. 2011). The samples have been carefully characterised to determine their size distributions, mineralogy and elemental compositions. The methods employed to characterise the samples are briefly described in the Appendix. A more complete description can be found in (James et al. 2016).

The particles are suspended in ethanol and delivered to the tungsten filament using a glass pipette. Typically a few particles (normally 5 or fewer) are deposited onto the filament for the four largest size bins. For the two smallest size bins, tens of particles are deposited. This implies that the evaporation curves recorded in each experiment are generally averages

of the evaporation profiles of a few particles within a size distribution (James, et al. 2016). The potential consequences of this are discussed in the following Section. A problem encountered in these experiments is liquid electromigration (Kumar, Howarth, & Dutta 2014), which causes the molten particles to move on the surface of the filament; this is particularly critical for studying the evaporation of refractory elements. In order to maintain the particles within the homogeneous temperature region of the filament (away from the electrodes), the surface needs to be roughened by carrying out several preparatory experiments (i.e. particles are melted and evaporated to leave a residue which roughens the surface, but the data is discarded). Also, the video camera is used to demonstrate that the particles ablate within the region where the temperature is measured by the pyrometer, approximately at the centre of the filament (Bones, et al. 2016).

The novelty of the MASI with respect to these previous experiments is, first, the capability of prescribing and controlling with a very good accuracy any kind of heating profile, including realistic atmospheric entry temperature curves obtained from the momentum and energy balance equations (Love & Brownlee 1991; Vondrak, et al. 2008). Secondly, the MASI is able to follow the evaporation process online with a very good time resolution (4 ms). And thirdly, the use of LIF in the UV-vis enables an extremely sensitive detection of many important elemental constituents of IDPs. Besides Na, Fe and Ca, other elemental constituents such as Mg, K, Al and Ni are easily observable by atomic fluorescence. Elements expected to evaporate in molecular form (SiO, AlO) can be also detected by LIF. Although the focus is on the observation of evaporation rates to constrain CABMOD, the atomic yields from different atmospheric entry temperature profiles (dependent on velocity, mass, and entry angle) can also be determined by running the experiments multiple times with high temperature curves to achieve full evaporation of residuals.

3. Results

3.1. Sample characterisation

Fig. 2, panels *b-d*, show examples of IDP analogues employed in this study, which have similarities and differences with MMs and S-IDPs. Ordinary chondrite (OC) fragments consist of compact aggregates (Fig. 2b), while the carbonaceous chondrites are very heterogeneous, showing porous fine-grained aggregates (Fig. 2c) not too different from the IDP assemblages (Jessberger, et al. 2001) as well as occasional coarse grains (Fig. 2d). Fig. A1 shows compositional maps of an OC H5 particle, which illustrates the heterogeneous distribution of elements in these meteoritic aggregates, analogous to what is usually found in MMs (Dobrică et al. 2012), S-IDPs (Brunetto et al. 2011) and cometary material (Brownlee et al. 2006). The particle in Fig. A1 has a Mg-rich silicate backbone with major Na-plagioclase and metallic Fe or iron sulfide (FeS) inclusions, and minor K and Ca-rich domains. Note that Mg is missing in those domains where other elements are enriched. This heterogeneous distribution of elemental constituents is also found in the carbonaceous analogues (Fig. A2).

The average elemental compositions (mixing ratios relative to Si) of the mineral and meteorite samples employed in this work are shown in Table 2 alongside the corresponding standard deviations. The standard compositions of relevant meteorite groups are also shown (Hutchinson 2004). Samples of single minerals were found to be in agreement with their nominal compositions. The elemental compositions of the meteoritic samples were found to be within a factor of 2 of the average compositions of their respective groups. The Allende sample was found to be depleted in Fe, Mg and Na with respect to the average CV composition, which is in agreement with the original analysis of the meteorite (Clarke et al. 1971), although this particular piece is very depleted in Ni. The analysis of the Murchison

sample yielded an average CM composition, in very good agreement with the original analysis (Fuchs, et al. 1973). Chergach is depleted in Fe and Ni with respect to the average H composition. Although large variability was observed in the Chergach samples – and in particular for Na in the smallest size bin– differences across size fractions were found to be non-significant, and therefore Table S2 only shows averages of the measurements of particles of different sizes.

3.2. Linear heating

The results of typical series of experiments with Chergach and Allende samples are shown in Fig. 3 (Na and Fe) and Fig. 4 (Na and Ca). Inspection of these figures reveals that Na, Fe and Ca ablate differentially, that is, evaporate at different times during the heating program. In this first group of experiments, a linear temperature ramp between 1400 and 2700 K is used in order to facilitate identification of major trends and simplify comparison to CABMOD simulations ($T = c_1 + c_2\ t$, with c_1 = 1375 K and c_2 = 138 K s^{-1}). In the Ca experiments, the ramp typically ends in a plateau at 2400 K to limit the electromigration of particles. Examples of evaporation curves of Na, Fe and Ca for all the meteorites and minerals considered in this study are shown in Fig. 5 (53 μm < R < 75 μm). For each element, there is a clear correspondence of the signal appearance temperature in experiments with the meteoritic analogues, and the appearance temperature in experiments with minerals which are rich in a particular element.

3.2.1. Sodium and Iron experiments

The melting point of olivine is used as a reference, taking the Mg/(Mg+Fe) ratio measured for each meteoritic analogue (Table 2). Fig. 3 shows that both Na and Fe start evaporating below the melting point of Fo_{80} olivine (1930 K) and even below Fo_{50} olivine

(1800 K), and that the Na peak appears at lower temperatures than Fe. The figure also indicates that the appearance temperatures of both Na and Fe (i.e. the temperatures at which each element is first observed to exceed the experimental detection limit) increase with particle size (Fig. 6 shows average appearance temperatures for all the experiments carried out in this study). The respective Na and Fe appearance temperatures for albite (Ab_{95}) and forsterite (Fo_{90}) are close to the melting point corresponding to their respective stoichiometry. The Na appearance temperature in Chergach is the same as for albite, and for Fe is consistent with the presence of metallic Fe (both known constituents of H5 meteorites). In Allende (CV3) and Murchison (CM2), the appearance temperatures of Na and Fe are consistent with sodic feldspathoids and metallic Fe, respectively.

Another way of visualising the dependence of the evaporation curves on size is to calculate the fractions of evaporated Na and Fe below certain reference temperatures, e.g. the melting points of Fo_{50} and Fo_{80} olivine (Fig. 7). The ratio Fe(T<1930K)/Fe(total) for Chergach reaches 15% for the smallest sizes. Chergach contains magnesium rich olivine (Fo_{83}), but as an H5 meteorite it also contains substantial amounts of metallic Fe, which explains why Fe evaporates below 1930 K. The ratio Fe(T<1800K)/Fe(total) is smaller than ~5% for all particle sizes. Na(T<1930K)/Na(total) is very significant for the three smallest size bins, which is an indication of low melting point Na-bearing minerals such as albite (in H chondrites), and sodalite and nepheline (in CM and CI chondrites). There is a strong size-dependence of the fraction ablated below the forsterite melting temperature. Some experiments were carried out with samples of Chergach prepared from reground large particles (R > 177 μm), which were subsequently segregated into the same size bins. For these, the fraction Na(T<1930 K)/Na(total) is smaller, which indicates preferential accumulation of the sodium-containing mineral in the smallest size bins during the primary size segregation.

A caveat to the interpretation of the evaporation curves in Fig. 3 - 5 is that the size bins employed in this study have relatively broad, overlapping size distributions (Fig. A3). This implies that when running many experiments for a single size bin, the characteristics of the release curves such as their appearance temperature, temperature at the maximum evaporation rate and full width at half maximum (FWHM) will show some scatter, as can be seen in Figs. 6 and 7. On the one hand, this is advantageous because experiments frequently involve the evaporation of several particles (see above), which has an averaging effect. But on the other hand there is some ambiguity in the assignment of the release curve FWHM, especially for minor elements such as Na and Ca. The release curve width is an especially important metric in the calibration of CABMOD, as will be shown in Section 4.

The Na release curves frequently consist of a superposition of different peaks, which one may assign to different particles. However, it turns out that one single particle (as registered by the video camera) may also produce composite release curves, as shown in Fig. 8, panel *b*. The reason for this is related to the Na-rich domains shown in Fig. A1 and A2, which will be discussed in more detail in Section 4.1. Fig. 9, panel *b*, shows an example for a bulk Allende sample where the Na peaks from several particles overlap (the video shows more particles than Na peaks in this case), while panel *a* shows a mixture of narrow and broad peaks which possibly result from several particles with several Na-rich grains (no video recording in this case). Fig. 9 *b* shows an example with a bulk Allende sample and with white aggregate particles (calcium-aluminium rich inclusions, or CAI) (separated by hand using a microscope from the rest of the Allende fragments). The bulk samples show lower appearance temperatures for Na. Fig. 10, shows examples for Murchison where (*a*) one or (*b*) two particles released Na. In Fig. 10*b* the video revealed two particles very close to each other, but never in contact.

In order to obtain a single set of parameters for each experimental run that can be compared with those of other samples, the strategy followed for Na has been fitting multiple peaks when the Na release curve is obviously a superposition and use the FWHM of the largest peak. The average results for a specific temperature ramp are shown in Fig. 6*b* and 6*e*, and indicate narrower Na peaks for Murchison, although the number of measurements is much smaller due to the limited amount of sample available. Another important caveat is that for the smallest size bin it is impossible to deposit just a handful of particles. In fact, tens of particles are deposited at least, which upon melting end up coalescing under the influence of electromigration. Therefore, the peak width in this case likely reflects other processes such as diffusion within much bigger particles than initially deposited. Note that although the width of these peaks does not correspond to the evaporation of Na from single particles, the appearance temperature is reliable because at that point the backbone silicates have not yet melted.

In the case of Fe, the situation is complicated by the obvious presence of a lower and a higher temperature phase, which overlap and generate the broad evaporation curves in panels *a* of Fig. 8, Fig 9 and Fig. 10 (i.e. the observation is common to the three meteoritic analogues). For illustrative purposes, the Fe signal in Fig. 8-10 has been fitted with a superposition of two Gaussian peaks. However, this is not always possible, and therefore we have refrained from carrying out a two peak decomposition analysis for all datasets. In many experiments the high temperature peak is better fitted by an asymmetric peak or a combination of several Gaussian peaks. The empirical fits indicate that the appearance temperature of Fe evaporating from this phase is consistent with forsteritic olivine (~2000 K). The FWHM and temperature at the maximum of the peaks of the meteoritic analogues, plotted in Fig. 6*e* and 6*f* respectively, are taken directly from the observed signal. Fig. 6*e* shows that the FWHM of the olivine Fo_{90} peaks is roughly half that of the meteoritic

analogue peaks. Fig. 6*f* shows that the temperatures at the maxima of Fo_{90} is very close to the temperature of the maxima for Allende and Chergach, suggesting that the major Fe containing phase is a silicate not far from Fo_{90}. Comparison of panels *b* (red and black curves) and *e* (pink curve) in Fig. 5 reinforces the idea that the high temperature peak of the meteoritic analogues is a silicate peak. The low temperature phase can be identified with metallic Fe by looking at the appearance temperature (Fig. 6*d*), although Fig. 5 shows that pure Fe particles produce peaks with higher temperature maxima.

3.2.2. Sodium and Calcium experiments

As a refractory element, Ca presents a big experimental challenge. There is a risk of particles moving out of the high temperature region of the filament due to electromigration before they ablate completely. This has been addressed by roughening of the filament surface (Kumar, et al. 2014) and by employing a video camera to screen out invalid experiments where particles move too far away from the centre. Fig. 4 shows examples of Na and Ca evaporation profiles obtained for the Chergach and Allende analogues for 3 size bins. The dashed and dash-dotted vertical black lines mark the 1800 K (Fo_{60}) and 1950 K (Fo_{80} and An_{90}) melting temperatures. It can be seen that for meteorite analogues, Ca starts evaporating not far from the appearance temperature in experiments with labradorite and anorthite (Fig. 5). The average Ca appearance temperature for labradorite is 2400 ± 120 K (n = 12) while the average Ca appearance temperatures for Chergach and Allende are respectively 2280 ± 120 K (n = 29) and 2210 ± 50 K (n = 9).

Multiple evaporation peaks are usually observed, which is reminiscent of the Na behaviour, although the individual peaks are generally narrower (with FWHM of the order of 20 K for the 138 K s^{-1} ramp). Fig. 11 shows 4 snapshots of the video corresponding to the experiments with the Chergach IDP analogue shown in Fig. 8, panel *b*. This sequence shows

how the four particles present on the surface of the filament in this experiment melted and moved a few millimetres before evaporating. The movement took place within the 'safe' region where there are no temperature gradients (Bones, et al. 2016). The particles A-D evaporating in frames 1-4 correspond to the Ca peaks in Fig. 8 panel *b*. The Ca peaks (Fig. 11, panel *b*) line up in time with the final decrease in intensity of the thermal emission of each particle (panel *a*). This illustrates how Ca (and most likely Al) remain in the particle until the particle's almost complete evaporation. There is more than one route to multiple peaks. Single particles have been observed to split after melting, which is the case of the experiment illustrated in Fig. 8, panel *b*, corresponding to the video frames in Fig. 11. In a frame previous to the frame1 in Fig. 11, a single particle is observed to split into two small and two large particles, which then migrate and evaporate sequentially in the order of smallest to largest. More frequently, several of the particles originally deposited evaporate individually. The case of the experiment with Allende in Fig. 9, panel *b* (thick lines), is more complex, with 6 initial particles; two of them split, but subsequent electromigration facilitated coalescence of some of the sub-particles with the main ones. About 5 small particles and two large particles are observed to evaporate within the field of view of the video camera. The evaporation of the small particles is responsible for the relatively low temperature of the onset of the Ca signal (~2300 K), while the main signal increase at 2700 K is due to the ablation of the two large particles.

3.3. Atmospheric entry profiles and elemental yields

Experiments performed using mass-specific entry heating profiles obtained from the CABMOD energy and momentum balance calculations (Vondrak, et al. 2008) are shown in Fig. 12 (for Fe and Na). The experiments simulate the entry of ordinary and carbonaceous chondrite particles with an average radius of 64 μm, speeds of 14, 17 and 21 km s^{-1} and entry

angle of 35°. Here, instead of plotting signal vs. time, the correspondence between time and altitude calculated by the model is used to provide a more intuitive representation of the atmospheric injection of Na and Fe by meteoric ablation. These plots provide a useful visualization of the process of atmospheric differential ablation: while the Na evaporation rate does not follow the temperature profile in any of the cases presented (it ablates completely before reaching the maximum particle temperature), the iron evaporation rate follows closely the temperature profile for the 14 km s^{-1} experiments. In this case evaporation stops because the temperature decreases, not because Fe is consumed. By contrast, for an entry speed of 21 km s^{-1}, Fe evaporation ends before the temperature starts decreasing, meaning that it has completely ablated from the particle.

In these experiments, the remaining Na and Fe (and Ca) fractions in the residual were determined by heating again the tungsten filament at a high temperature to completely vaporize the residual as shown in Fig. 13, panels *b* and *d*. For the particular experiments in Fig. 12 with Allende (bottom row of panels), it is observed that full evaporation of Na occurred in the 3 cases, while 20%, 80% and 100% of Fe ablated with increasing speed. Table 3 lists the yields of Na, Fe and Ca (i.e. the ablated fraction) from heating experiments of the three meteorite analogues using calculated heating profiles for several combinations of particle mass and velocity (all for 35° entry angle). The table shows that the yields increase with speed and mass, and that the Na yield is 100% for almost all combinations except for the smallest particles at the lowest two velocities. Also included in the table are yields of Ca from experiments using linear heating ramps, showing a decrease with particle size. A caveat to these calculations is that the design of the MASI requires prescribing modelled atmospheric heating profiles to the particles. The modelled atmospheric heating profiles depend on the free molecular drag and the free molecular heat transfer coefficients (Vondrak, et al. 2008). Therefore, uncertainties propagating from these parameters or from the simplifications

involved in the energy and momentum balance equations are not taken into account in the calculation of atmospheric entry yields.

4. Discussion

4.1. Interpretation of the evaporation profiles and elemental yields

The relative abundances of the oxides of the major elemental constituents in carbonaceous chondritic material, i.e. SiO_2, MgO and FeO, are located in the olivine field of the solidus ternary diagram, very close to Fo_{50} olivine at the quasi-binary solution intersection (Wu, et al. 1993). This suggests that complete and uniform melting following the olivine phase diagram would be a reasonable assumption provided that a solid IDP was well represented by a single olivine grain. However, because of the excess of SiO_2 with respect to MgO and the presence of the minor components CaO and Al_2O_3, some enstatite, Ca-pyroxene (diopside), and Al silicate and oxide co-exist with olivine, and melting starts at the corresponding peritectic point (located at ~1600 K for FeO-MgO-SiO_2 (Bowen & Schairer 1935)). Furthermore, from Fig. A1 and A2 it is obvious that in spite of the silicate component of chondrites being stoichiometrically close to olivine, they are far from being a homogeneous material, but consist of different grains of different compositions. In previous partial heating experiments with Allende and Murchison (Jurewicz, Mittlefehldt, & Jones 1993) it has been found that equilibration at low temperature is an extremely slow process that depends on solid state diffusion in olivine. This means that it is more likely that volatile components like FeS (eutectic point at ~1300 K (Walder & Pelton 2005)) and albite (melting point at ~1400 K (Bowen 1913)) melt earlier than the silicate backbone, which is what the present experiments suggest.

4.1.1. Sodium

Na-rich feldspar grains ~20 μm in size have been reported for Chergach (Weisberg, et al. 2008). The average feldspar in an H chondrite is Ab_{82} (Bryan & Kullerud 1975). These small plagioclase grains are separated from the matrix in the grinding process and most likely accumulate in the smallest size bins, while the largest bins are dominated by coarser grained minerals. The preferential accumulation of fine plagioclase grains in the small size bins is confirmed by the smaller Na(T<1930 K)/Na(total) observed for samples prepared from reground large particles (Fig. 7). The appearance temperatures for the smallest size bins are close to those observed for albite. Plagioclase grains still exist in larger size bins, but they are embedded in larger particle aggregates. Considering the low porosity of H5 meteorites (Wilkison & Robinson 2000) it is likely that the whole particle needs to melt in order to release the inner sodium-rich pockets, which may cause the observed delayed evaporation for larger size particles. A recent study of unmelted and partially melted micrometeorites collected at the Earth's surface shows that the porosity of partially melted particles is higher, which is likely an indication of low temperature melting and evaporation of volatile mineral phases creating empty pockets within the IDP grainy aggregates (Kohout et al. 2014). The higher porosity of Allende (Macke, Consolmagno, & Britt 2011) could be an explanation of the somewhat weaker size dependences observed.

The Na appearance temperatures from Murchison and Allende are higher than for Chergach, which reflects the higher melting temperature of nepheline, which is the major Na-bearing feldspatoid in carbonaceous chondrites. The limited number of experiments carried out with Murchison samples show well defined, narrower and sharper profiles than seen in the experiments with Allende.

4.1.2. Iron

The Fe-rich distinct grains that can be seen in Fig. A1 are probably enclosed in small pockets as well, and may require the melting of surrounding material to be released, which could explain the size dependence of the Fe appearance temperatures. The abundance of Fe also makes the evaporation profiles somewhat more regular and smoother than for Na, and the presence of lower and higher temperature phases produces the very long melting curves shown in Figs. 8-10. Chondritic materials are assemblages of different metal alloys and minerals, such as Fe-Ni metal grains, FeS, and silicates of varying Fe content. Thus, it is not surprising that the appearance temperature of Fe is not far from the melting point of metallic Fe (~1800 K). Fig. 5 shows that, in contrast, Mg-rich olivine samples Fo_{90} (pink line in panel *e*) display Fe vapor appearance temperatures around 200 K higher than the meteoritic analogues, and that the later can be qualitatively understood as a superposition of the metallic Fe and Fo_{90} evaporation curves. Carbonaceous chondrites are poor in metallic Fe, but a Fe residual is expected to start depositing upon reaching the eutectic point of the FeS phase diagram at ~1300 K (Tachibana & Tsuchiyama 1998; Walder & Pelton 2005). The fraction of Fe ablated below the melting point of the corresponding Mg-rich olivine is higher for Chergach, which is consistent with the higher content of metallic Fe in H-type ordinary chondrites (Jarosewich 1990). The observation that silicate peaks in the meteoritic analogues are more asymmetric and wider than the olivine peaks, but similar to the pyroxene peaks, hints at the presence of both types of silicates, and it also suggests that the composition of melts at the peritectic point of the FeO-MgO-SiO_2 system (Wu, et al. 1993) favours initially enhanced Fe evaporation rates.

Table 3 shows that Fe complete evaporation occurs at larger size and higher speed than for Na, which proves that these elements ablate differentially. Because meteoritic particles are only observed to fully melt around 1900 K, Na differential ablation is not the result of

chemically fractionation of an equilibrated melt, but of the independent melting and evaporation of minerals more volatile than the major silicate components.

4.1.3. Calcium

Anorthite, a major Ca-bearing mineral in chondrites (Bryan & Kullerud 1975; Clarke, et al. 1971; Fuchs, et al. 1973) melts at ~1900 K (Bowen 1913), not far from the temperature of the olivine liquidus. Therefore, it seems in principle more likely that CaO would equilibrate with the FeO-MgO-SiO_2 melt. Then, considering the high sensitivity of Ca evaporation to the composition of the melt (Hashimoto 1983), it would seem plausible to expect a delayed release of Ca from a chondritic melt with high MgO content when compared to a separate anorthite grain which is free of Mg. The distribution of Ca between the different pseudo-species in an equilibrated melt depends on the thermodynamic activities of MgO, SiO_2 and Al_2O_3, and therefore evaporation of Ca is very dependent on composition, and not only on the vapour pressure law parameters of CaO (Fegley & Cameron 1987). However, the appearance temperatures of Ca in the IDP analogues are close to those in the Ca-rich plagioclase references (e.g. Fig. 5), which do not contain Mg. Fig. 4 shows that the Ca appearance temperature is dependent on the particle size, and that the smallest size, with an appearance temperature of 2200K, is the closest to the anorthite evaporation onset.

Fig. 11 illustrates an experiment in which the evaporating particle split into 4 sub-particles, which subsequently evaporated according to their size, with the smallest particle disappearing first. Fragmentation of melted droplets of a scale observable by the video camera only occurred in a small fraction of the experiments, but this phenomenon provides insight into the sensitivity of refractory material evaporation to particle size. Calcium peaks can be lined up closely with the complete evaporation of the particles, which indicates that Ca is one of the last elements to evaporate (Hashimoto 1983). The activity of CaO is dependent

on the activities of MgO and SiO_2. The smaller the particles are, the less time it takes to evaporate their major components, which in turn implies that the CaO activity will rise accordingly. This corresponds to the transition between phases III and IV in Hashimoto's chondritic melt evaporation sequence (Hashimoto 1983), where the melt becomes closer to a Ca-rich plagioclase stoichiometry. The low appearance temperature and smooth increase of the Ca signal in some experiments (e.g. Fig. 9*b*) can be also traced back to the evaporation of very small particles observed in the video recordings. The experimental constraint of working in the MASI with particle size bins (particle size distributions are shown in Fig. A3) is therefore an important limitation for deriving of Ca yields for discrete particle sizes.

Table 3 shows that Ca does not completely evaporate under any atmospheric heating profile. Major Ca- and Al-containing minerals melt at similar temperatures to Fe-poor olivine and pyroxene, and equilibrated FeO-MgO-SiO_2-CaO-Al_2O_3 melts may form. Therefore, differential ablation of Fe with respect to Ca results to a large extent from chemical fractionation within such melts. The fraction of Fe present as metal-sulfide evaporates independently due to the low melting temperature and the immiscibility of metallic Fe with silicates at low pressures. The table also shows that the Ca yields from Allende are generally larger than those from Chergach for atmosphetic profiles (except in one case), and agree for linear temperature ramps. The smaller fraction of Mg found in our Allende sample compared to bulk CV composition (Table 2) may be partly responsible for the earlier release of Ca from Allende. This effect becomes less important for hotter temperature profiles like the linear ramps, which produce larger Ca evaporated fractions than the atmospheric profiles.

4.2. Assessment of CABMOD results

CABMOD has been adapted to model the MASI experiments by using the temperature profiles measured by the pyrometer instead of the temperature from momentum and energy

balance calculations. The model is then run with the specific elemental composition and density of the different IDP analogues employed. Key assumptions in CABMOD and previous chemical ablation modelling efforts are: i) IDPs melt completely and uniformly, ii) the melt remains homogeneous at all times, iii) the vapour and melt are in thermodynamic equilibrium and iv) the rate of evaporation of a species into a vacuum is equal to the rate of evaporation needed to balance the rate of uptake in a closed system (i.e. Langmuir evaporation) (McNeil, Lai, & Murad 1998; Vondrak, et al. 2008). In order to satisfy the first and second assumptions the composition of the particles has to be simplified. 'Olivine' composition is assumed, meaning that other phases known to exist in IDPs need to be somehow integrated in the idealized material. Crucially, the fraction of Fe present as metal sulfide needs to be accounted for as FeO, either by assuming that all the particle mass is made out of a CI silicate, or by re-computing the FeO fraction in the silicate from the total Fe elemental abundance, which results in a silicate with excess FeO. This Section examines the validity of these three assumptions in view of the experimental results. The comparison with the model helps to gain new insights into how the evaporation process takes place.

Fig. 14 shows a comparison between the MASI Na, Fe and Ca evaporation curves obtained for one particular size bin (53 μm < R < 75 μm) for Chergach and Allende with a linear temperature ramp and the corresponding predictions using the original version of CABMOD published by (Vondrak, et al. 2008) (hereafter referred to as CABMOD-1) with olivine melting points corresponding to their respective FeO/MgO ratios (2000 K for Chergach and 1800 K for Allende and Murchison, indicated by thick black vertical lines on each panel). CABMOD-1 (in blue) is unable to reproduce the appearance temperature and the width of the evaporation profiles. The dependence on particle size (average radius of the corresponding size bin) of the FWHM and the temperature at the maximum evaporation calculated with CABMOD-1 are plotted in Fig. 6 (dashed lines in panels *b*, *c*, *e* and *f*). The

poor agreement between CABMOD-1 profiles and MASI observations in Fig. 14, and more generally between the modelled and observed evaporation peak parameters plotted in Fig. 6 as a function of particle size, is primarily an indication of the inadequacy of the aforementioned assumptions i) and ii) for meteoritic analogues. It has been shown that Na, Fe and Ca evaporation onsets in IDP analogues can be understood in terms of the melting of at least three single mineral phases included in the meteoritic aggregates: albite, metal-sulfide, and Ca-containing silicate. Implementing a multi-phase aggregate in CABMOD constrained by the MASI experimental data will be the subject of future work.

4.2.1. Sodium

In a first attempt to improve the agreement between CABMOD and the MASI results for Na, we upgraded the model (hereafter CABMOD-2) with the latest version of the MAGMA code, which includes revised data for Na and K aluminosilicates (Holland & Powell 2011). Revision of the standard Gibbs free energies of Na-bearing aluminosilicate melts resulted in lower equilibrium vapour pressures and thus in a lower evaporation rate (see E1), which results in a better fit to the high temperature tail of the Na peaks. However, simulations still produced Na peaks significantly narrower and delayed with respect to the MASI observations in Fig.2.

In order to account for the lower appearance temperature of the Na signal, the sigmoidal temperature dependence of the phase transition factor f(T) given by E2 can be made wider by increasing the value of the parameter τ. For any given melting temperature T_c (e.g. the midway temperature between the solidus and liquidus lines in the olivine phase diagram), increasing τ is equivalent to relaxing the constraint imposed on Na evaporation by the narrow phase transition range of olivine. Thus, the problem of the simplistic description of the composition of the particle is provisionally addressed in CABMOD-2 for Na by

allowing for a wider solid-liquid transition temperature range. This could be regarded as a way of dealing with the lower-lying liquidus boundaries of FeO-MgO-CaO-SiO_2 systems in the presence of Na_2O (Biggar & Humphries 1981; Pan & Longhi 1990), which would determine the onset of Na evaporation if the material was fully equilibrated. A narrower sigmoid does a better job with Allende Na profiles, but this is just to compensate for the lower melting point of the Allende olivine. The comparison between model runs for Na and observations shown in Fig. 14, although still far from perfect, highlights the fact that the Na evaporation rate is significantly slower than CABMOD-1 was predicting. For the linear temperature ramp employed throughout this work, the FWHMs of the peaks modelled with CABMOD-2 are now in reasonable agreement with the MASI results (Fig. 6*b*). The position and width of the modelled peaks with respect to the observations suggest that the sticking coefficient γ_{Na} cannot be much lower than 1.0.

The CABMOD-2 calculations of Na evaporation rates from micrometeorite entries are in reasonable agreement with the MASI simulations in Fig. 12, where the experimental and calculated curves are normalized to the same area.

4.2.2. Iron

CABMOD is not a multiphase model and therefore does not capture the low temperature peak observed in the Fe evaporation curves. Fig. 14 illustrates that the model does a slightly better job in reproducing the Fe profile shapes for Allende than for Chergach, which is most likely due to the lower metallic content in carbonaceous meteorites. The modification of the phase transition parameters in CABMOD-2 does not have a very large impact on the Fe modelled curves (cf. the red and blue curves in Fig. 6*b* and 6*e* – in the latter case they fully overlap). This is because the equilibrium vapour pressure of Fe above olivine is very small at temperatures close to the melting point. CABMOD-2 does not predict strong

dependences of the evaporation curve parameters (appearance temperature, width and temperature at the peak) on particle size.

The modelled Fe evaporation peaks for Chergach are in very good agreement with the olivine Fo_{90} observations, which is demonstrated by the good match in terms of FWHM and temperature at the maximum shown in Fig. 6*e* and 6*f*. The CABMOD profiles for meteoric IDP analogues in Fig. 14 give a much better match to the experimental olivine data than the experimental meteoritic data, which is not too surprising considering that the model material for IDPs in CABMOD is actually Mg-rich olivine. In addition, this indicates that the sticking coefficient (γ_{Fe}) for Fo_{90} olivine cannot be much lower than 1.0, since otherwise the maximum of the evaporation curves would be shifted to significantly higher temperatures. A sticking coefficient of 0.24 for Fe and FeO (Alexander 2002) would shift the peaks to higher temperatures as indicated by the red square symbol in Fig. 6*f* (corresponding to the grey curve in Fig. 14*e*). The silicate Fe peaks of the meteoritic samples are wider and more asymmetric than the pure olivine ones: they reach their maxima at similar temperature (~2300 K, Fig. 6*f*) and show a similar termination, but the evaporation rate from meteoritic silicate between 2000 K and 2200 K is higher. Superposed evaporation of particles of different sizes, for example a combination of the green, red and pink peaks in Fig. 6e) cannot be invoked to explain this difference, because olivine samples show almost identical size distributions to the meteoritic analogues, and because molten droplets appear to behave in the same manner with respect to electromigration, coalescence and splitting. We have also found that the different choices to include metallic Fe as extra FeO in the silicate or simply ignoring the metallic phase and assuming that all the particle is made out of olivine with the observed FeO fraction (the default mode of CABMOD) does not significantly change the shape of the modelled silicate peak with respect to the meteoritic analogue data.

We find that Fe starts evaporating at lower temperatures from melts with the Fe-rich peritectic FeO-MgO-SiO_2 composition at ~1600K, but perhaps the most reasonable explanation for the shape of the meteoritic silicate peaks is the loss of effective evaporation surface as the particles melt. When aggregate particles melt completely, they lose surface area, first because of the filling in of pores and irregularities (Fig. 2b and 2c), as well as dehydration cracks and vessicles formed at lower temperatures from the volatilization of water and sulfur (Toppani, et al. 2001); and second, because the liquid surface in contact with the filament does not contribute to evaporation. Then it is plausible to infer that before complete melting at ~1900 K the liquid surface available for evaporation is significantly larger than that of a sphere of equivalent radius, and then shrinks abruptly to that of a molten droplet. For dense crystalline material (e.g. Fig. 2*c*) the phase transition should cause a less dramatic reduction in surface, which explain the good match between olivine peaks and the CABMOD results. A general caveat for all types of particles is that CABMOD assumes spherical symmetry, when in MASI molten particles rest on a surface and therefore are oblate spheres. Experiments with two cameras looking from the top and the side of the vacuum chamber show that the radius to height ratio for stationary liquid particles is 1, while for moving particles (electromigration kicks off around 2100 K) the particles wet more surface and show ratios of the order of 2. This implies that CABMOD generally overestimates the particle surface in MASI experiments, and explains why Fe evaporation terminates at higher temperatures than predicted. Future modelling of MASI benchmarking experiments will incorporate knowledge on particle size and shape.

Improved prediction of the Fe evaporation rates can be achieved by including a metal component in the model at the fraction by weight dictated by the assumed composition (e.g. H and CV in Fig. 14). Since metallic Fe melts earlier and is immiscible in molten silicate, the fraction of metallic Fe can be accounted for as an independent phase, and its vapour pressure

(Desai 1986) and evaporation rate can be computed separately. The evaporation rate of Fe from the metal phase can then be added to the silicate Fe evaporation rate to get a total Fe evaporation rate, as shown in in Fig. 14, panels *b* and *c* (pink lines). This approach works strikingly well for the low temperature Fe peak assuming that the metallic Fe phase is divided into small particles of around 5 μm in radius (peak labelled "200"), which is consistent with what compositional mapping shows (Figure A1). It does not work well if all metallic Fe is assumed to be contained in a single lump (the peak labelled with "1"). This is not because Fe evaporates faster from smaller particles, but because they are consumed faster and the peak evaporation rate occurs at a lower temperature. There is good evidence from the South Pole Water Well MM collection that molten sulfides coalesce to the surface of fully melted cosmic spherules forming one characteristic metal bead at the leading edge (Taylor et al. 2011). Such migration and coalescence likely result from the density difference between the molten metal-sulfide droplets and the silicate phase under strong deceleration, while MASI only simulates evaporation from a melt with no comparable forces applied to the particles. On the other hand, partially molten MMs show multiple beads. The expected atmospheric entry scenario for the Fe-bearing metal-sulfide phase in IDPs should be intermediate between curves labelled "200" and "1", because only a fraction of incoming IDPs form cosmic spherules (Carrillo-Sánchez, et al. 2015). A Fe metallic-sulfide phase will be implemented in the follow-up development of CABMOD and will be reported elsewhere.

4.2.3. Calcium

Fig. 14 shows the CABMOD-2 predictions for Ca evaporation from Chergach and Allende analogues (panels *c* and *f*, respectively). It can be seen that CABMOD-2 does not replicate in general the appearance temperature and the shape of the curves. The calculation for the smaller size bins produces the right sequence of the observed peaks in Fig. 14*c*: the

smaller simulated particle (green) shows a lower Ca appearance temperature than the bigger one (red), consistent with the observed particle fragments A and B evaporating earlier and being smaller than C and D (see Fig. 11 for reference). It can be inferred that because all particles are fragments of the original particle, their Ca signal rising edges occur at lower temperature than the modelled Ca peak. Fig. 14*f* shows an example where the main rising edge is well matched by the model. According to the video recording, the main Ca peak correspond to the evaporation of two of the particles originally deposited in the filament. The low temperature Ca signal corresponds to the evaporation of ~5 small particles which were deposited originally on the filament or split from larger particles. The green curve, which corresponds to a simulation of a smaller particle, shows a lower onset and is in qualitative agreement with the low temperature tail of the MASI signal.

We have argued that because of the dependence of CaO activity on other species that vaporise at lower temperatures, the size of the particle determines the appearance temperature of the Ca vapour. In order to perform a more realistic modelling of the MASI data, CABMOD-2 calculations should be run on a set of particle sizes sampled from the size distributions in Fig. A3. However, because the objective of MASI is simulating atmospheric entry and because it is preferable to reduce the complexity of the model, it seems more appropriate to try to narrow down the size distribution of the particles or to develop the capability of estimating the mass of individual particles for each experiment. These are tasks that should be addressed in further developments of the MASI.

4.3. Elemental yields and differential ablation

Given that 75 % of IDPs are estimated to be carbonaceous (Taylor, et al. 2012), the Allende phase change parameterisation is employed for calculations of atmospheric evaporation profiles with CABMOD-2 which are then used to derive Fe and Ca yields

relative to Na. It is thought that CM chondrites such as Murchison are mineralogically closer to IDPs. However, because the MASI is a destructive technique and our supply of Murchison samples was limited, and since this meteorite yields similar results to Allende at this stage, the latter is taken as the standard IDP analogue in the rest of the study. Few micrometeorites have been found with the same specific mineralogical features of the CV3 matrix (fayalitic olivine, smectite, Ni-bearing sulfides) (Genge 2010). However, to a first-order approximation these compositional nuances do not have a very large impact on the evaporation rates of major elemental components, considering that CM and CV bulk compositions are very close to each other in the ternary FeO-MgO-SiO_2 ternary diagram (Jarosewich 1990). A more important caveat from the point of view of Fe evaporation is that while sulfur is present in carbonaceous chondrites mainly in the form of sulfate (Burgess, Wright, & Pillinger 1991), this is a very minor component of S-IDPs, MMs and cometary dust, where sulfur appears in the form of FeS (Jessberger, et al. 2001; Zolensky & Lindstrom 1992; Zolensky et al. 2006). Even if the sulfur depletion observed in S-IDP is not caused by atmospheric entry, a considerable amount of Fe (~30% according to the elemental abundances published by (Arndt et al. 1996), or equivalently ~8% wt (Taylor, et al. 2011)) will still be associated with sulfur.

Despite the slower Na evaporation rates obtained from CABMOD-2 (e.g. Fig. 14, top panel row) resulting from the upgrade of MAGMA and the changes in the phase transition factor, the difference from the Na yield predicted by CABMOD-1 is small. The only consequences of the broader Na evaporation peak are then related to the generation of meteoroid head echoes and radar detection, which will be the subject of a future study. The relative yields obtained with Allende can be scaled to CI to obtain results more representative of the total meteoritic input. Modification of the Na peak shape does not have a significant

influence on the position of the mesospheric sodium layer because vertical mixing by eddy diffusion is comparatively rapid in the upper mesosphere.

The experimentally-determined and modelled yields of Na and Fe for a selection of velocity- and mass-specific calculated heating profiles are shown in Table 4. The data shows some scatter, and there are some disagreements which are possibly related to the higher yield of Fe at lower temperatures due to FeS and metallic Fe. Nevertheless, the model reproduces correctly the trend of greater Fe evaporation with increasing particle speed and mass, as shown by the differential ablation coefficients (DAC = ratio of the fraction of ablated Fe to the ratio of ablated Na). Thus CABMOD-2 provides a reasonable estimate of the differential ablation of Na and Fe for different combinations of mass and size, even if the detailed physics of melting of a complex aggregate of mineral grains is not described currently in the model. As discussed above, CABMOD attributes differential ablation exclusively to chemical fractionation in a melt of chondritic composition (Schaefer & Fegley Jr 2004b). MASI experiments indicate that the differential ablation of volatile components results from partial melting of low temperature phases that do not equilibrate with the olivine backbone, and chemical fractionation in the silicate is responsible for differential ablation of the most refractory elements.

We can derive a mass and velocity distribution-weighted DAC for Fe and Ca relative to Na from the data in Table 3 by using the Zodiacal Cloud model (Nesvorný, et al. 2011) (velocity and mass weighting factors included in Tables 4 and 5). For the Fe/Na DAC, this results in CI-normalized values of 8.4 and 7.1 for the MASI and CABMOD-2 respectively. This good agreement arises because most of the mass in the Zodiacal Cloud mass distribution is in the 36 and 64 μm radius bins. Because most of the Na and Fe are released in the range of masses and velocities considered, the results are not too far from the Fe/Na DAC derived

from CABMOD-2 considering the full Zodiacal cloud mass and velocity distributions, which is 6.9.

Global modelling of the lidar-observed sodium and iron layers in the terrestrial mesosphere requires a Fe/Na DAC of 3.5 (Carrillo-Sánchez, et al. 2015). The MASI results indicate that complete Na evaporation occurs for almost all combinations of mass and speed. Moreover, it seems that Fe ablates slightly more efficiently than expected due to the low temperature phase unaccounted for by CABMOD-2. Therefore, the remaining difference between the CABMOD-2 predicted DAC and that derived from lidar observations and modelling (Carrillo-Sánchez, et al. 2015) implies both differential ablation and enrichment of Na in meteoroids relative to CI, as suggested in previous studies (Trigo-Rodriguez & Llorca 2007) and observed in cometary material (Schulz et al. 2015).

Experimental and modelled Ca yields and Ca/Na DACs are listed in Table 5. The large difference between the CABMOD-2 Ca/Na DAC for the full velocity and mass distributions (0.078) and for the set of selected mass and velocity combinations in the table (0.014) is due to the absence of larger masses and velocities. This reduced set of velocities and masses is imposed by experimental constraints on the range of temperatures currently accessible with MASI (the range of the pyrometer as well as the movement of particles out of the field of view caused by electromigration). The heating profiles corresponding to the missing tail of speeds and masses reach the highest temperatures, and therefore are those for which the largest yields of Ca occur. It is then noticeable that the experimental Ca/Na DAC for the limited set of low speeds and masses considered is 0.06, not far from the full distribution modelled result of 0.078. This poor agreement for Allende (Ca/Na DAC = 0.014 for CABMOD-2 vs 0.064 from the MASI), results from the high Ca yield in experiments for R = 100 μm and v=14 km s^{-1}, which has a large weighting in the DAC calculation. By

contrast, the yields of Ca at high speeds predicted by CABMOD-2 for the three smallest size bins are much larger than the observations, but these combinations have low weightings in the calculation. The yields of Ca from Chergach particles in Table 3 are generally lower, in particular for the R = 100 μm and v=14 km s^{-1} combination. For large evaporated fractions (i.e. as in linear temperature ramps), the Chergach and Allende Ca yields do not differ – divergence is apparent when the evaporated fractions are only a few percent, as is the case in atmospheric ablation.

Overestimated Ca yields may be explained by the need to work with size distributions rather than monodisperse samples. For a given size distribution, the presence of particles smaller than the average may increase the Ca yield with the small signals appearing below the expected threshold as discussed in Section 4.2.3. The specific composition of the IDP analogues employed may also have an impact on the release of Ca, particularly regarding the relative abundances of Mg and Si. Since a larger abundance of Ca relative to Mg and Si is the case in CAIs, some experiments were carried out with hand-sorted CAI fragments in order to check for differences in the evaporative behaviour of Ca, but the results were inconclusive (e.g. Fig. 9). The inconsistencies highlighted above suggest that in future work with refractory material it may be more useful to employ synthetic CI particles of prescribed CaO content (e.g. (Hashimoto 1983)) to determine the Ca yields with better precision, perhaps combined with an attempt to reduce the width of the size distributions or working with single particle experiments. The general conclusion of the present work is that for the range of most frequent entry speeds and masses the fraction of Ca evaporated is lower than 10%, which is in line with the predictions of CABMOD, the lidar observations of the mesospheric Ca layer and the lack of depletion of Ca in stony cosmic spherules as opposed e.g. to Fe (Brownlee, Bates, & Schram 1997).

An important remark is that the the present experimens have been carried out under very low O_2 concentration, with log fO_2 < -9.4. Oxygen fugacity in the region of the atmosphere where IDPs ablate is between log fO_2 = -6 and log fO_2 = -8 and oxidation of Fe-rich phases is demonstrated by the magnetite shells found in most MMs (Toppani, et al. 2001). Under our conditions, the magnetite-magnesioferrite spinel solid solution is not stable (Toppani & Libourel 2003), which may reduce the temperature onset of melting and evaporation of Fe with respect to atmospheric conditions. Future experiments with the MASI will address the effect O_2 fugacity within the relevant atmospheric range.

5. Conclusions

A novel experimental set up has been constructed to test the description of meteor ablation in the widely used chemical ablation model CABMOD. Fig. 15 shows the measured and calculated evaporation rates of Na, Fe and Ca expressed as a linear density (atoms evaporated per meter), scaled to their relative evaporation efficiencies (Na=1). CABMOD reproduces the general features of the MASI experiments, such as the relative position of the evaporation curves and the position of the maximum evaporation of Na and Ca. CABMOD also reproduces Fe/Na differential ablation. The current version of CABMOD produces reliable results for the integrated differential ablation of Fe and presumably of the other major elemental constituents of similar volatility such as Mg and Si, which will be the subject of future research with the MASI. On the other hand, the integrated differential ablation of Ca is not well described. The inconsistencies between the Ca simulations and experiments, and between experiments with different analogues, point to the high sensitivity of Ca evaporation to particle size and composition, and suggest the use of synthetic analogues with a more homogeneous size and Ca content to improve precision. In any case, we found that the

average Ca ablated fraction for carbonaceous and ordinary chondrites particles with radii ≤100 μm and entry speeds ≤31 μm is ~4 %.

CABMOD-1 does a poor job in matching the width of the Na and Fe peaks, and the magnitude of the Ca ablation relative to Na, i.e. instantaneous properties of single meteors that may be important for radar detection. A temporary solution for the Na profile has been found by increasing the width of the temperature-dependent phase transition factor (CABMOD-2). This could help in the current efforts to better model radar head echoes and reduce uncertainties in the simulation of observed radar meteor rates. Due to its low ionization potential and high volatility, ablated Na is a major contributor to radar detectability of meteors. A decrease of the peak number of head echo electrons due to the slower Na ablation would correspond to a quadratic decrease of the radar cross section, which could imply that the radar detection limit actually corresponds to larger and faster particles (Janches, et al. 2014; Janches, et al. 2015). These calculations are relevant to quantifying the input rate of cosmic dust into the Earth's atmosphere, as well as the injection rate of ablated metals. Further developments of CABMOD need to address the complexity of the IDP composition and morphology identified in the present work and resolve the influence of these on differential ablation rates.

Acknowledgements. This work was supported by the European Research Council (project number 291332 – CODITA). J.M.T-R acknowledges funding received from Spanish Ministry of Science (research projects AYA 2011-26522 and AYA 2015-67175). The MASI and CABMOD data sets are available upon request to J.M.C.P.

Table 1. List of reference minerals and meteorites used to prepare IDP analogues

Material	Composition	Density /g cm^{-3}	Melting point /K	Application	Origin
Aegirine	$NaFeSi_2O_6$	3.5	1300	LIF Fe/Na calibration	Mount Malosa, Malawi [a]
Albite	$Ab_{95}An_5$	2.6	1380	Reference for OC	Skarvebergbukten, Seiland, Finmark, Norway[b]
Labradorite	$Ab_{45}An_{55}$	2.6	1530	LIF Ca/Na calibration Reference for OC and CC	Unknown [b]
Anorthite	Ab_3An_{97}	2.7	1830	Reference for OC and CC	Japan [b]
Olivine	$Fa_{10}Fo_{90}$	3.3	2030	Anhydrous coarse grained IDP analogue Reference for OC and CC	Almeklovdalen, Sunnmør, Norway[b]
Pyroxene	$Fs_{15}En_{85}$	3.3	1720	Anhydrous coarse grained IDP analogue Reference for OC and CC	Colorado, USA [a]
Iron	99.8% Fe	7.87	1800	Reference for OC and CC Pyrometer calibration Metalic IDP analogue Reference for OC and CC	Goodfellow Cambridge Ltd.
Chergach[c]	OC (H5) Fe in metallic form: 57%. 100×MgO/(MgO+FeO) = 85% Na: Ab_{82} (grains of ~20 μm).	3.5		OC IDP analogue	Erg Chech, Timbuktu district, Mali. Fall: 2 or 3 July 2007 [a]
Allende[d]	CC (CV3) 100×MgO/(MgO+FeO) = 62% Fe: phyllosilicates, olivine, pyroxene Na: sodalite, nepheline Ca: anorthite, augite, gehlenite	2.9		CC IDP analogue.	Allende, Chihuahua, Mexico. Fall: 8 February 1969 [e]
Murchison[f]	CC (CM2) 100×MgO/(MgO+FeO) = 67% Fe: phyllosilicates, olivine, pyroxene Na: nepheline Ca: anorthite, augite, gehlenite	2.9		CC IDP analogue	Murchison, Victoria Australia. Fall: 28 September 1969 [e]

[a] Purchased from mineral and meteorite dealers. [b] University of Leeds, School of Earth and Environment Research Collections. [c](Weisberg, et al. 2008). [d] (Clarke, et al. 1971)
[e] Institut de Ciències de l'Espai (CSIC) research collection. [f](Fuchs, et al. 1973; MacPherson et al. 1983)

Table 2. Atomic mixing ratio relative to Si of samples employed in this study and reference meteoritic compositions.(Hutchinson 2004)

Material	**Fe**	**Mg**	**Na**	**K**	**Ca**	**Al**	**Ni**
Aegerine	0.55 ± 0.11	<l.o.d [a]	0.45 ± 0.11	<l.o.d	0.033 ± 0.008	<l.o.d	<l.o.d
Albite	0.0024 ± 0.0019	0.006 ± 0.004	0.33 ± 0.04	0.005 ± 0.002	0.015 ± 0.007	0.344 ± 0.013	<l.o.d
Labradorite	<l.o.d	<l.o.d	0.17 ± 0.04	0.010 ± 0.004	0.21 ± 0.04	0.54 ± 0.01	<l.o.d
Anorthite	0.024 ± 0.013	<l.o.d	0.015 ± 0.010	<l.o.d	0.50 ± 0.09	0.89 ± 0.02	<l.o.d.
Olivine	0.19 ± 0.08	1.74 ± 0.09	<l.o.d	<l.o.d	trace	Trace	0.012 ± 0.006
Pyroxene	0.15 ± 0.07	0.83 ± 0.09	trace	trace	0.021 ± 0.012	0.10 ± 0.02	<l.o.d.
Allende [b]	0.445	0.608	0.012[c]	trace	0.043	0.082	trace
Murchison [b]	0.775	0.901	0.04	0.002	0.062	0.096	trace
Chergach	0.44 ± 0.08	0.98 ± 0.09	0.06 ± 0.03[d]	0.002 ± 0.003	0.06 ± 0.02	0.09 ± 0.03	0.007 ± 0.008
CV	0.759	1.071	0.026	0.001	0.085	0.117	0.042
CM	0.819	1.047	0.039	0.002	0.069	0.096	0.045
H	0.819	0.959	0.046	0.003	0.052	0.069	0.046

[a] Limit of detection. [b] The standard deviation of ICP-AES measurements is below 5% for all major elemental components. [c] Allende SEM Na/Fe = 0.03 (±10%); MASI signal calibrated with known amounts of albite and olivine gives Na/Fe = 0.04 (±30%). [d] Chergach SEM Na/Fe = 0.14 (±50%); MASI signal calibrated with aegirine gives Na/Fe = 0.14 (±20%)

Table 3. Na, Fe and Ca yields (Φ_{Metal} = Ablated/Total) from experiments with the Chergach, Allende and Murchison IDP analogues

			Allende (CV3)								**Chergach (H5)**								**Murchison (CM2)**							
***R*[a] /µm**	***m*[b] /µg**	***v* /km s^{-1}**	Φ^{MASI}_{Na}	σ[c]		Φ^{MASI}_{Fe}	σ	***n*[d]**	Φ^{MASI}_{Ca}	σ	Φ^{MASI}_{Na}	σ	***n***	Φ^{MASI}_{Fe}	σ	***n***	Φ^{MASI}_{Ca}	σ	Φ^{MASI}_{Na}	σ	***n***	Φ^{MASI}_{Fe}	σ	***n*[e]**	Φ^{MASI}_{Ca}	σ
9	0.01	14	0.01	0.01	2	0.00	0.02																			
		17	0.14	0.03	4	0.00	0.02																			
		21	0.85	0.06	3	0.46	0.20																			
		31	0.95	0.03	2	0.80	0.13	4	0.05	0.03	0.97	0.02				3	0.006	0.005								
		41	0.97	0.02				5	0.06	0.04	0.97	0.02				4	0.20	0.13								
		ramp 2[f]	1.00	0.02				3	0.83	0.18	1.00	0.02				4	0.8	0.3								
36	0.57	14	0.90	0.09	5	0.52	0.08	1	0.02										0.94		1	0.97				
		17	0.95	0.05	5	0.41	0.28	1	0.02										0.99		1	0.93				
		21	0.97	0.01	4	0.52	0.19	3	0.04	0.02	0.97	0.02				4	0.007	0.007	1.02		1	0.91				
		31	0.94	0.00	2	0.67	0.45	3	0.05	0.04	0.97	0.02				3	0.03	0.03								
		ramp 1[g]									1.00	0.02				2	0.4	0.3	1.00	0.02				3	0.4	0.3
		ramp 2	1.00	0.02				4	0.5	0.4	1.00	0.02				4	0.6	0.4								
64	3.18	14	0.95	0.07	5	0.58	0.17	1	0.01		0.93	0.08	2	0.98	0.01				0.94		1	0.99				
		17	0.97	0.03	4	0.88	0.16	6	0.03	0.03	0.97		1	0.97		3	0.00	0.01	0.92		1	1.00				
		21	0.97	0.02	5	0.88	0.14	5	0.06	0.04	0.96		1	0.98		3	0.00	0.01	0.94		1	1.01				
		ramp 1	1.00					1	0.08		1.00					1	0.04		1.00					1	0.24	
		ramp 2	1.00	0.02				2	0.14	0.14																
100	12.15	14	0.95	0.09	3	0.91	0.05	2	0.23	0.05	1.00	0.02				2	0.02	0.01								
		17	0.99	0.03	3	0.95	0.04	1	0.32																	

[a] Average radius. [b] Average mass assuming spherical particles with density 3 g cm^{-3}. [c] Standard deviation. [d] Number of measurements Fe + Na experiments. [e] Number of measurements Ca + Na experiments. [f] Ramp 2: temperature ramps in Fig. 4. [g] Ramp 1: temperature ramps in Fig 3.

Table 4. Fe and Na yields (Φ_{Metal} = Ablated/Total) and Differential Ablation Coefficients (DAC = Φ_{Fe}/Φ_{Na}) from MASI experiments with the Allende IDP analogues, and from CAMOD-2 calculations (entry angle 35°).

R [a] /μm	m [b] /μg	v /km s^{-1}	n [c]	Φ_{Na}^{MASI}	σ [d]	Φ_{Na}^{CABMOD}	Φ_{Fe}^{MASI}	σ	Φ_{Fe}^{CABMOD}	DAC $_{MASI}$ [e]	σ	DAC $_{CABMOD}$	v weight [f]	DAC $_{MASI}$ [g]	DAC $_{CABMOD}$	m weight [f]	DAC $_{MASI}$ [h]	DAC $_{CABMOD}$
9	0.01	14	2	0.01	0.01	0.00	0.00	0.02	0.00	0		0.0	0.15	**0.44**	**0.09**	0.45		
		17	4	0.14	0.03	0.01	0.00	0.02	0.00	0		0.0	0.075					
		21	3	0.85	0.06	1.00	0.46	0.20	0.02	20	9	0.8	0.025					
		31	2	0.95	0.03	1.00	0.80	0.13	1.00	31	5	37.4	0.0025					
36	0.57	14	5	0.90	0.09	1.00	0.52	0.08	0.05	21	4	1.9	0.15	**8.46**	**5.08**	1		
		17	5	0.95	0.05	1.00	0.41	0.28	0.60	16	11	22.5	0.075					
		21	4	0.97	0.01	1.00	0.52	0.19	1.00	20	7	37.4	0.025					
		31	2	0.94	0.00	1.00	0.67	0.45	1	27	18	37.4	0.0025					
64	3.18	14	5	0.95	0.07	1.00	0.58	0.17	0.49	23.0	7	18.3	0.15	**6.11**	**5.79**	0.52		
		17	4	0.97	0.03	1.00	0.88	0.16	1.00	34	6	37.4	0.075					
		21	5	0.97	0.02	1.00	0.88	0.14	1	34	5	37.4	0.025					
100	12.15	14	3	0.95	0.09	1.00	0.91	0.05	1	36	4	37.4	0.15	**5.67**	**6.53**	0.37		
		17	3	0.99	0.03	1.00	0.95	0.04	1	36	2	37.4	0.075					
																	20.7±2.1	**17.5**
																	8.4	**7.1**
																	5.6	**4.7**
																		5.9
																		6.9
																		3.5

Mass- and velocity-weighted Fe DAC relative to Na, Allende (entry angle α=35°)

Mass- and velocity-weighted Fe DAC relative to Na, normalized to CI (entry angle α=35°)

Mass- and velocity-weighted Fe DAC relative to Na, normalized to CI, 1.5 Na enrichment (entry angle α=35°)

CABMOD-1 (previous version (Carrillo-Sánchez, et al. 2015)) integrated DAC **for all possible *m*, *v* and *α***

CABMOD-2 (updated version, this work) integrated DAC **for all possible *m*, *v* and *α***

DAC derived from lidar observations (chemistry effects accounted for)(Carrillo-Sánchez, et al. 2015)

[a] Average radius. [b] Average mass assuming spherical particles with density 3 g cm^{-3} [c] Number of measurements for each (v, m) combination. [d] Standard deviation. [e] Velocity distribution-weighted DACs for each (m, v) combination. [f] Weighting factors from the Zodiacal Cloud mass and velocity distributions (Nesvorný, et al. 2011; Nesvorný, et al. 2010). [g] Mass distribution-weighted DACs for each mass bin. [h] Overall DACs.

Table 5. Na and Ca yields (Φ = Ablated/Total) and Differential Ablation Coefficients (DAC = Φ_{Ca}/Φ_{Na}) from experiments with the Allende IDP analogues, and from CAMOD-2 calculations (entry angle 35°).

R^a /µm	m^b /µg	v /km s^{-1}	n^c	Φ_{Na}^{MASI}	σ^d	Φ_{Na}^{CABMOD}	Φ_{Ca}^{MASI}	σ	Φ_{Ca}^{CABMOD}	DAC $_{MASI}$ ^{e}	σ	DAC $_{CABMOD}$	v weight^f	DAC $_{MASI}$ ^{g}	DAC $_{CABMOD}$	m weight^f	DAC $_{MASI}$ ^{h}	DAC $_{CABMOD}$
9	0.01	14				0.000			0.000			0	0.15	**0.00**	**0.00**	0.45		
		17				0.008			0.000			0	0.075					
		21				1.000			0.000			0	0.025					
		31	4	0.97	0.02	1.000	0.05	0.03	0.027	0.19	0.13	0.1	2.5×10^{-3}					
		41	4	0.97	0.02	1.000	0.06	0.04	0.686	0.25	0.15		2.5×10^{-4}					
36	0.57	14	1	1.00 ^{i}	0.02	1.000	0.02		0.000	0.08		0	0.15	**0.03**	**0.01**	1		
		17	1			1.000	0.02		0.000	0.06		0	0.075					
		21	3			1.000	0.04	0.02	0.003	0.14	0.06	0	0.025					
		31	3			1.000	0.05	0.04	0.924	0.2	0.1	3.3	2.5×10^{-3}					
64	3.18	14	1			1.000	0.01		0.000	0.04	0.00	0	0.15	**0.02**	**0.03**	0.52		
		17	6			1.000	0.03	0.03	0.001	0.11	0.09	0	0.075					
		21	5			1.000	0.06	0.04	0.361	0.2	0.2	1.3	0.025					
100	12.15	14	2			1.000	0.23	0.05	0.000	0.8	0.2	0	0.15	**0.16**	**0.01**	0.37		
		17	1			1.000	0.32		0.010	1.1		0.04	0.075					
																	Mass- and velocity-weighted Ca DAC relative to Na, Allende (entry angle α=35°)	**0.2±0.1**	**0.05**
																	Mass- and velocity-weighted Ca DAC relative to Na, normalized to CI (entry angle α=35°)	**0.06**	**0.01**
																	Mass- and velocity-weighted Ca DAC relative to Na, normalized to CI, 1.5 Na enrichment (entry angle α=35°)	**0.04**	**0.01**
																	CABMOD-1 (previous version (Carrillo-Sánchez, et al. 2015)) integrated DAC **for all possible *m*, *v* and α**		0.06
																	CABMOD-2 (updated version, this work) integrated DAC **for all possible *m*, *v* and α**		0.08
																	DAC derived from lidar observations (chemistry effects accounted for)(Carrillo-Sánchez, et al. 2015)		0.04

^{a} Average radius. ^{b} Average mass assuming spherical particles with density 3 g cm^{-3} ^{c} Number of measurements for each (v, m) combination. ^{d} Standard deviation. ^{e} Velocity distribution-weighted DACs for each (m, v) combination. ^{f} Weighting factors from the Zodiacal Cloud mass and velocity distributions (Nesvorný, et al. 2011; Nesvorný, et al. 2010). ^{g} Mass distribution-weighted DACs for each mass bin. ^{h} Overall DACs. ^{i} Average Na yield for all experiments in the following rows.

APPENDIX: CHARACTERIZATION OF IDP ANALOGUES AND MINERAL SAMPLES

Bulk Elemental Composition

Scanning Electron Microscopy with Energy Dispersive X-ray spectroscopy (SEM-EDX) was used to determine the relative elemental compositions of Chergach and mineral samples across different size fractions (SEM Jeol JSM-6610LV coupled to an Oxford Instruments INCA X-max80 EDS). An array of particles with a thin gold coating was placed in the SEM chamber, selecting a relatively flat surface on one particle and measuring the spectrum with 20 keV electrons. Spectra were measured for multiple particles (5 to 7 measurements for each material).

The elemental composition of the Allende and Murchison samples was analysed by an ICP-AES (Inductively coupled plasma - atomic emission spectroscopy) ICAP 6500 Thermo Electron for major elements and an ICP-MS (Inductively coupled plasma mass spectrometry) Thermo Electron XSeries II for minor and trace elements. Solutions were prepared from approximately 0.025 g of each sample fluxed with 0.05 g of Li-metaborate and dissolved in 30 ml HNO_3 1N and 1 drop of HF. Four standard reference materials provided by the US Geological Survey were used for external calibration; internal calibration of the equipment was carried out before the measurements and rhodium was used as internal standard. Three determinations of the elemental composition were carried out and averaged for each meteorite, showing standard errors lower than 5% for most elements.

SEM Textural analysis and compositional maps

Particle topography and homogeneity, both within each particle and across whole samples, was assessed using SEM (FEG-SEM – FEI Nova 450) with EDX (AMTEK) at 18 kV). Fig. 2 shows micrographs of several particles of Chergach and Allende. These

demonstrate the naked eye observation of Allende samples being made up of several distinct particle types, whereas Chergach is more homogeneous. In general, Chergach and some Allende particles are relatively compact, whilst the remainder of Allende particles are porous aggregates rather more reminiscent of IDPs (Dobrică, et al. 2009; Mackinnon & Rietmeijer 1987). Fig. A1 and A2 show micrographs and co-located EDX maps for a particle of Chergach and Allende respectively. Both meteorite samples display widespread Mg and Fe, related to their mafic silicate constituents. In the Chergach sample several Fe rich domains are clear, likely representing Fe-Ni metal grains, as well as sulfide (FeS). In addition, domains are clearly visible where Na is present and Mg and Fe absent, most likely plagioclase feldspar in Chergach and feldspathoid minerals in Allende. K is present in Chergach associated to Na (orthoclase). Ca rich domains are also evident (feldspar, pyroxene and phosphates in Chergach; gehlenite and anorthite in Allende), associated to Na in some areas (feldspar in Chergach).

Size Distributions

The size distribution of each particle bin has been assessed by analysing backlit optical microscope images of arrays of particles on a microscope slide as described by (James, et al. 2016). The measured size distributions of four of the Chergach sample size fractions and three of Allende are shown in Fig. A3. The mean radius of each size fraction in this case is well within the range defined by the sieves.

Figure captions

Figure 1. Top (panel *a*) and side (*b*) views of MASI.

Figure 2. IDP analogues. Panel *a*: cuvettes containing ground meteorite particles segregated according to mesh size. Panel *b*: Scanning Electron Microscopy (SEM) micrograph of an example Chergach IDP analogue. Panels *c* and *d*: Allende IDP analogues.

Figure 3. Laser Induced Fluorescence signal of Na (top panels) and Fe (bottom) for different particle size bins (radii indicated in the legend) of the Chergach (right) and Allende (left) meteoritic IDP analogues. The temperature ramp (black line) is plotted in the right hand side axis of each panel. The dashed and dash-dotted vertical black lines mark the 1800 K (Fo_{60}) and 1950 K (Fo_{80}) temperature thresholds.

Figure 4. Laser Induced Fluorescence signal of Na (top panels) and Ca (bottom) for different particle size bins (radii indicated in the legend) of the Chergach (right) and Allende (left) meteoritic IDP analogues. The temperature ramp (black line) is plotted in the right hand side axis of each panel. The dashed and dash-dotted vertical black lines mark the 1800 K (Fo_{60}) and 1950 K (Fo_{80} and An_{90}) temperature thresholds.

Figure 5. Selection of experiments for the size bin 53 μm < *R* < 75 μm with all the samples employed in this study. Top panel row (*a* - *c*): meteorites, including a run with white aggregate inclusions (CAIs) separated from Allende's black matrix. Bottom panel row (*d* - *f*): minerals: aegirine (dark yellow), albite (red), labradorite (cyan), enstatite (blue), anorthite (green), iron (black) and olivine (pink). Left column (panels *a* and *d*): Na signal; Central column (panels *b* and *e*): Fe signal; Right column (panels *c* and *f*): Ca signal.

Figure 6. Appearance temperatures (panels *a* and *d*), widths (FWHM) of the evaporation peaks (*b* and *e*) and temperature at the maximum evaporation (*c* and *f*) of Na (top panels) and Fe (bottom panels) for IDP analogues and minerals. The horizontal lines in panels *a* and *d* indicate the melting temperature of albite (Ab_{95}) (Bowen 1913), sodalite (Antao & Hassan 2002), nepheline (Bowen 1912), forsterite (Fo_{60}, Fo_{80}, Fo_{90}) (Bowen & Schairer 1935) and pure iron. The legends for panels *b* and *e* are shared with panels *c* and *f* respectively. Black, red, light green, blue and deep green symbols are for Chergach, Allende, Murchison, Fo_{90} olivine and En_{85} pyroxene respectively. Dashed lines: predictions of the previous version of CABMOD (1). Solid lines: predictions of the current version of CABMOD (2). Empty red squares: CABMOD-2 calculations with sticking coefficients for Fe and FeO set to 0.24. The FWHMs and temperatures at the maximum of the release curves are specific for the heating ramp in Fig. 3: $T = c_1 + c_2 \times t$, with c_1 = 1375 K and c_2 =138 K s^{-1}.

Figure 7. Fractions of Na (panel *a*) and Fe (panel *b*) ablated below a reference temperature T_0 (1800 K or 1930 K for the melting points of Fo_{50} and Fo_{80} olivine, respectively) relative to the total Fe and Na ablated.

Figure 8. Panel *a*: detection of Na (red) and Fe (blue, 10 point moving average) in an experiment with Chergach analogues of the 53 μm < *R* < 75 μm size bin for a 138 K s^{-1} linear heating ramp. Multi-peak Gaussian fits of Na (black) and Fe (green) are shown. The individual fitted peaks are shown by dashed lines. Panel *b*: the same for another experiment where Na (red) and Ca (blue) were detected. This particular example corresponds to a single particle experiment. The video frames in Fig. 11 show that the particle fragments A-D sequentially ablate.

Figure 9. Panel *a*: detection of Na (red) and Fe (blue) in an experiment with Allende analogues of the 53 μm < *R* < 75 μm size bin for a 138 K s^{-1} linear heating ramp. Multi-peak

fits of Na (black) and Fe (green) are shown. Individual Gaussian peaks fitted to the data are shown by dashed lines. Panel *b*, solid lines: the same for another experiment where Na (red) and Ca (blue) were detected. This example corresponds to an experiment with six particles; two of the initial particles split, at least four sub particles coalesced, and five small and two large paricles evaporated within the field of view of the video camera. Panel *b*, dotted lines: experiment with one of the white aggregate particles found in the Allende matrix, which have been identified as CAIs (Clarke, et al. 1971).

Figure 10. Panel *a*: detection of Na (red) and Fe (blue, 10 point moving average) in an experiment with Murchison analogues of the 53 μm < *R* < 75 μm size bin for a 138 K s^{-1} linear heating ramp. Multi-peak fits of Na (black) and Fe (green) are shown. The individual fitted peaks are shown by dashed lines. Panel *b*: the same for another experiment where Na (red) and Ca (blue, 10 point moving average) were detected. This example corresponds to an experiment with two particles, one of which is observed to ablate within the field of view of the video camera.

Figure 11. Snapshots of a video corresponding to the experiment in Fig. 8, panel *c*. Frame 1 shows four particles around the centre of the filament, where the circular target of the pyrometer is positioned. At this point all the sodium has been already shed by the particles and particle A is ablating. Frame 2 shows the evaporation of particle B while particles C and D have moved past the target. In Frame 3 particles C ablates and particle D is starting to ablate. In Frame 4 particle D ablates and to its left a remnant of C is still visible. The plots show the correlation of light intensity emitted by each particle recorded by the video camera (panel *a*) with Ca LIF evaporation peaks (panel *b*), plotted alongside the temperature measured by the pyrometer (panel *b*, right axis) . The dips in the green and red curves correspond to the passage of the particles C and D over the circle of the pyrometer target.

Oscillations in temperature occur when the particle is inside the target (e.g. Frame 1, corresponding to ~8.5 s). Evaporation occurs when the intensity of the particle drops rapidly (indicated by dashed lines).

Figure 12. Atmospheric ablation vertical profiles for R_{avg} = 60 μm particles at three different speeds and three different IDP analogues. Red lines are for observed Na LIF, blue lines for observed Fe LIF (bottom axes) and black lines for measured temperature (top axes). The Na and Fe ablation rates obtained from the updated version of CABMOD are the thick black solid and dotted lines, respectively. The observed and modelled Na (Fe) profiles are normalized to the same area. Pink dashed lines indicate the modelled Na ablation rate with the previous version of CABMOD (Na profiles are out of scale as indicated).

Figure 13. Example of experiment designed to determine the yield of Na and Fe from an atmospheric entry heating profile (panels (a) and (c)) corresponding to a 0.5 μg particle (size bin with radii between 19 and 53 μm) entering the atmosphere at 14 km s^{-1}. The lower limit of the pyrometer range (1300 K) impedes reproducing the full temperature profile from low temperature. However, the temperatures relevant for Na and Fe evaporation are within the accessible range. Panels (b) and (d) show the complete evaporation of the residual Na and Fe remaining in the material unablated in the atmospheric entry using a high temperature step function. The oscillations in high temperature profile are due to the difficulty of controlling temperature close to the upper limit of the pyrometer range (~3000 K). However, these oscillations do not have any influence on the result since the only requirement is that the residual particle fully ablates.

Figure 14. Na, Fe and Ca evaporation rates (in arbitrary units) vs. temperature (138 K s^{-1} ramp) for the 53 μm < R < 75 μm size bin. The left column shows data for Chergach (panels *a*, *b* and *c*) and the right column data for Allende (panels *d*, *e* and *f*). Each row shows data for

one element: Na (panels *a* and *d*), Fe (panels *b* and *e*) and Ca (panels *c* and *f*). Evaporation rates (units are atoms per second in CABMOD) normalized to an arbitrary scale are on the left axes and the temperature of the filament on the right axes. The black vertical lines indicate the melting temperatures of Fo_{80} and Fo_{60}. The prediction of CABMOD-1 and CABMOD-2 for the average radius of the 53 μm < *R* < 75 μm size bin (64 μm) appear in blue and red respectively. The green lines and cyan lines correspond to CABMOD-2 calculations for a smaller and a larger particle size respectively, using the same heating ramp. The pink lines correspond to two phase (metal + olivine) calculations. The gray line in panel e correspond to a calculation for Allende with *R* = 64 μm and assuming a sticking coefficient for Fe and FeO of 0.24 (Alexander 2002).The Ca peaks labelled with letters correspond to the particle evaporation in Fig. 11.

Figure 15. Ablation rates as in Fig. 12 for Allende particles at 17 km s^{-1} for Na (black and green), Fe (red) and Ca (blue). Experimental curves are the thin lines and CABMOD-2 simulations are thick lines. The Fe and Ca profiles cannot be obtained simultaneously, so the two corresponding Na profiles are plotted to demonstrate reproducibility. The target (dashed line) and measured (solid line) temperature profiles are shown in pink. The observed and modelled curves are scaled to their relative differential ablation coefficients for this particle mass and velocity.

Figure A1. Energy-dispersive X-Ray (EDX) analysis of an IDP analogue (Chergach, OC, H5), showing the spatial distribution of Na, Ca, K, Fe and Mg in the particle.

Figure A2. SEM micrograph and EDX maps of an example particle of Allende IDP analogue.

Figure A3. Size distributions of Chergach (a) and Allende (b) sample bins as measured by optical microscopy. Data have been normalised to give probability density functions for each distribution. The mean radius of each distribution is also marked.

References

Alexander, C. M. O. D. 2002, M&PS, 37, 245

Antao, S. M., & Hassan, I. 2002, CaMin, 40, 163

Arndt, P., Bohsung, J., Maetz, M., & Jessberger, E. K. 1996, M&PS, 31, 817

Biggar, G. M., & Humphries, D. J. 1981, MinMag, 44, 309

Bones, D. L., Gómez Martín, J. C., Empson, C., et al. 2016, RScI, 87, 094504

Borovicka, J. 1993, A&A, 279, 627

Bowen, N. L. 1912, American Journal of Science, Series 4 Vol. 33, 551

Bowen, N. L. 1913, AmJS, Series 4 Vol. 35, 577

Bowen, N. L., & Schairer, J. F. 1935, AmJS, Series 5 Vol. 29, 151

Brownlee, D., Tsou, P., Aléon, J., et al. 2006, Science, 314, 1711

Brownlee, D. E. 2016, Elements, 12, 165

Brownlee, D. E., Bates, B., & Schram, L. 1997, M&PS, 32, 157

Brunetto, R., Borg, J., Dartois, E., et al. 2011, Icarus, 212, 896

Bryan, W. B., & Kullerud, G. 1975, Metic, 10, 41

Burgess, R., Wright, I. P., & Pillinger, C. T. 1991, Metic, 26, 55

Carrillo-Sánchez, J. D., Plane, J. M. C., Feng, W., Nesvorný, D., & Janches, D. 2015, GRL, 42, 6518

Ceplecha, Z., Borovička, J., Elford, W. G., et al. 1998, SSRv, 84, 327

Clarke, R., Jarosevich, E., Mason, B., et al. 1971, in Smithsonian Contributions to the Earth Sciences (Washington: Smithsonian Institution Press)

Court, R. W., & Sephton, M. A. 2009, GeCoA, 73, 3512

Court, R. W., & Sephton, M. A. 2011, GeCoA, 75, 1704

Crank, J. 1975, The Mathematics of Diffusion (Oxford: Clarendon Press)

Desai, P. D. 1986, Journal of Physical and Chemical Reference Data, 15, 967

Dobrică, E., Engrand, C., Duprat, J., et al. 2009, M&PS, 44, 1643

Dobrică, E., Engrand, C., Leroux, H., Rouzaud, J. N., & Duprat, J. 2012, GeCoA, 76, 68

Fegley, B., & Cameron, A. G. W. 1987, E&PSL, 82, 207

Fuchs, L. H., Olsen, E., & Jensen, K. J. 1973, in Smithsonian Contributions to the Earth Sciences (Washington: Smithsonian Institution Press)

Greshake, A., Klöck, W., Arndt, P., et al. 1998, M&PS, 33, 267

Hashimoto, A. 1983, GeoqJ, 17, 111

Holland, T. J. B., & Powell, R. 2011, JMetG, 29, 333

Hutchinson, R. 2004, Meteorites (Cambridge, UK: Cambridge University Press)

James, A. D., Frankland, V. L., Alonso-Azcárate, J., et al. 2016, JASTP, doi:10.1016/j.jastp.2016.08.011

Janches, D., Dyrud, L. P., Broadley, S. L., & Plane, J. M. C. 2009, GRL, 36, L06101

Janches, D., Heinselman, C. J., Chau, J. L., Chandran, A., & Woodman, R. 2006, JGRA, 111, A07317

Janches, D., Plane, J. M. C., Nesvorný, D., et al. 2014, ApJ, 796, 41

Janches, D., Swarnalingam, N., Plane, J. M. C., et al. 2015, ApJ, 807, 13

Jarosewich, E. 1990, Metic, 25, 323

Jessberger, E., Stephan, T., Rost, D., et al. 2001, in Interplanetary Dust, eds. E. Grün, B. S. Gustafson, S. Dermott, & H. Fechtig (Springer Berlin Heidelberg), 253

Jurewicz, A. J. G., Mittlefehldt, D. W., & Jones, J. H. 1993, GeCoA, 57, 2123

Kohout, T., Kallonen, A., Suuronen, J. P., et al. 2014, M&PS, 49, 1157

Krinov, E. L. 1970, Metic, 5, 85

Kumar, P., Howarth, J., & Dutta, I. 2014, JAP, 115, 044915

Love, S. G., & Brownlee, D. E. 1991, Icarus, 89, 26

Love, S. G., & Brownlee, D. E. 1993, Science, 262, 550

Macke, R. J., Consolmagno, G. J., & Britt, D. T. 2011, M&PS, 46, 1842

Mackinnon, I. D. R., & Rietmeijer, F. J. M. 1987, RvGeo, 25, 1527

MacPherson, G. J., Bar-Matthews, M., Tanaka, T., Olsen, E., & Lawrence, G. 1983, GeCoA, 47, 823

Markova, O. M., Yakovlev, O. I., Semenov, G. A., & Belov, A. N. 1986, Geokhimiya, 11, 1559

McNeil, W. J., Lai, S. T., & Murad, E. 1998, JGRD, 103, 10899

McNeil, W. J., Murad, E., & Plane, J. M. C. 2002, in Meteors in the Earth's Atmosphere, eds. E. Murad, & I. P. Williams (Cambridge: Cambridge University Press), 265

Nesvorný, D., Janches, D., Vokrouhlický, D., et al. 2011, ApJ, 743, 129

Nesvorný, D., Jenniskens, P., Levison, H. F., et al. 2010, ApJ, 713, 816

Noguchi, T., Ohashi, N., Tsujimoto, S., et al. 2015, E&PSL, 410, 1

Notsu, K., Onuma, N., Nishida, N., & Nagasawa, H. 1978, GeCoA, 42, 903

Pan, V., & Longhi, J. 1990, CoMP, 105, 569

Plane, J. M. C. 1991, Int Rev Phys Chem, 10, 55

Plane, J. M. C. 2012, CSR, 41, 6507

Plane, J. M. C., Feng, W., & Dawkins, E. C. M. 2015, ChRv, 115, 4497

Richter, F. M., Davis, A. M., Ebel, D. S., & Hashimoto, A. 2002, GeCoA, 66, 521

Safarian, J., & Engh, T. A. 2012, MMTA, 44, 747

Sandford, S. A., & Bradley, J. P. 1989, Icarus, 82, 146

Schaefer, L., & Fegley Jr, B. 2004a, EM&P, 95, 413

Schaefer, L., & Fegley Jr, B. 2004b, Icarus, 169, 216

Schulz, R., Hilchenbach, M., Langevin, Y., et al. 2015, Nature, 518, 216

Tachibana, S., & Tsuchiyama, A. 1998, GeCoA, 62, 2005

Taylor, S., Alexander, C. M. O. D., Delaney, J., et al. 2005, GeCoA, 69, 2647

Taylor, S., Jones, K. W., Herzog, G. F., & Hornig, C. E. 2011, M&PS, 46, 1498

Taylor, S., Matrajt, G., & Guan, Y. 2012, M&PS, 47, 550

Taylor, S., Messenger, S., & Folco, L. 2016, Elements, 12, 171

Toppani, A., & Libourel, G. 2003, GeCoA, 67, 4621

Toppani, A., Libourel, G., Engrand, C., & Maurette, M. 2001, M&PS, 36, 1377

Trigo-Rodriguez, J. M., & Llorca, J. 2007, AdSpR, 39, 517

Trigo-Rodriguez, J. M., Llorca, J., Borovička, J., & Fabregat, J. 2003, M&PS, 38, 1283

Vondrak, T., Plane, J. M. C., Broadley, S., & Janches, D. 2008, ACP, 8, 7015

Walder, P., & Pelton, A. D. 2005, Journal of Phase Equilibria and Diffusion, 26, 23

Wang, J., Davis, A. M., Clayton, R. N., Mayeda, T. K., & Hashimoto, A. 2001, GeCoA, 65, 479

Weisberg, M. K., Smith, C., Benedix, G., et al. 2008, M&PS, 43, 1551

Wilkison, S. L., & Robinson, M. S. 2000, M&PS, 35, 1203

Wu, P., Eriksson, G., Pelton, A. D., & Blander, M. 1993, ISIJI, 33, 26

Zolensky, M. E., & Lindstrom, D. 1992, in Lunar and Planetary Science (Houston: Lunar and Planetary Institute), 161

Zolensky, M. E., Zega, T. J., Yano, H., et al. 2006, Science, 314, 1735

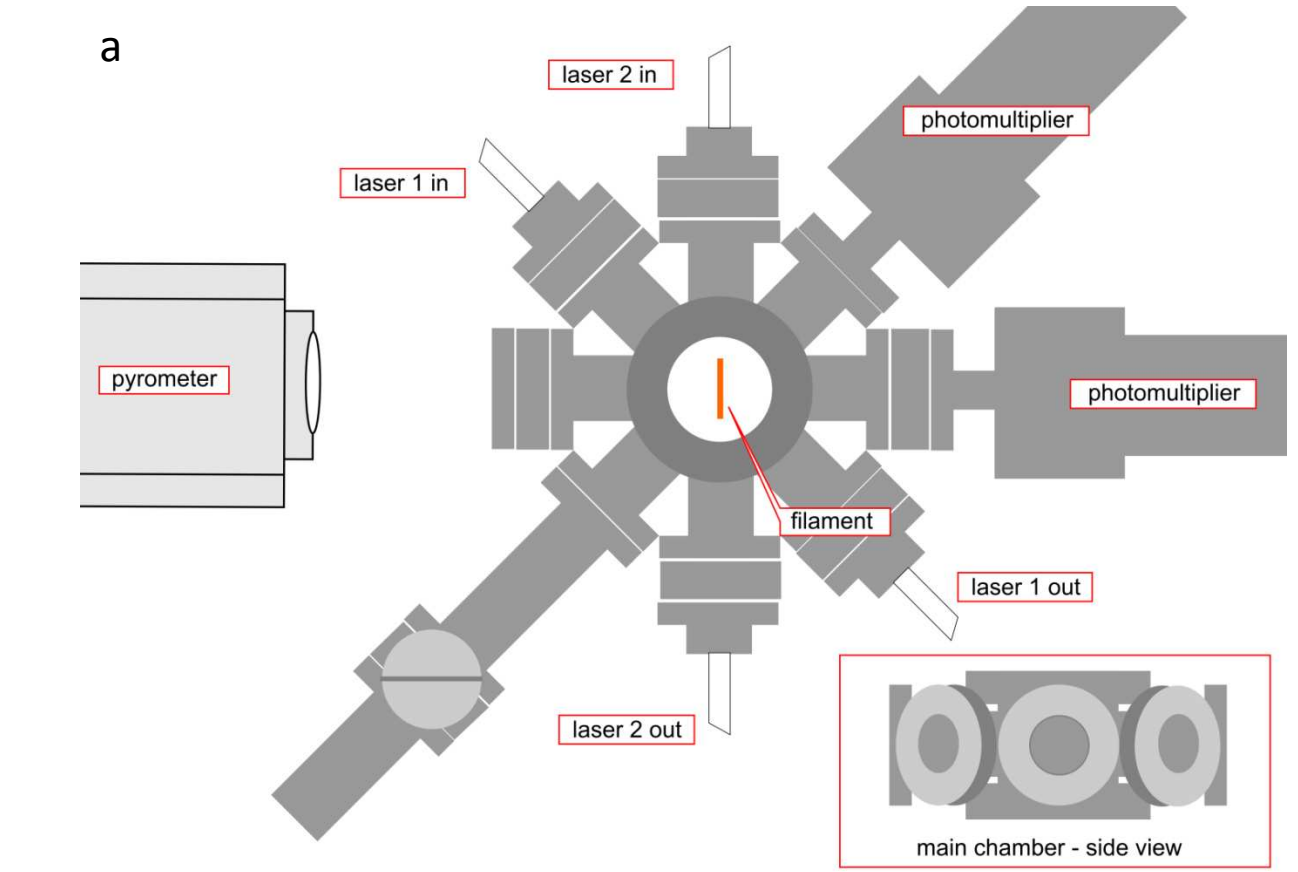
a
laser 2 in
photomultiplier
laser 1 in
pyrometer
photomultiplier
filament
laser 1 out
laser 2 out
main chamber - side view

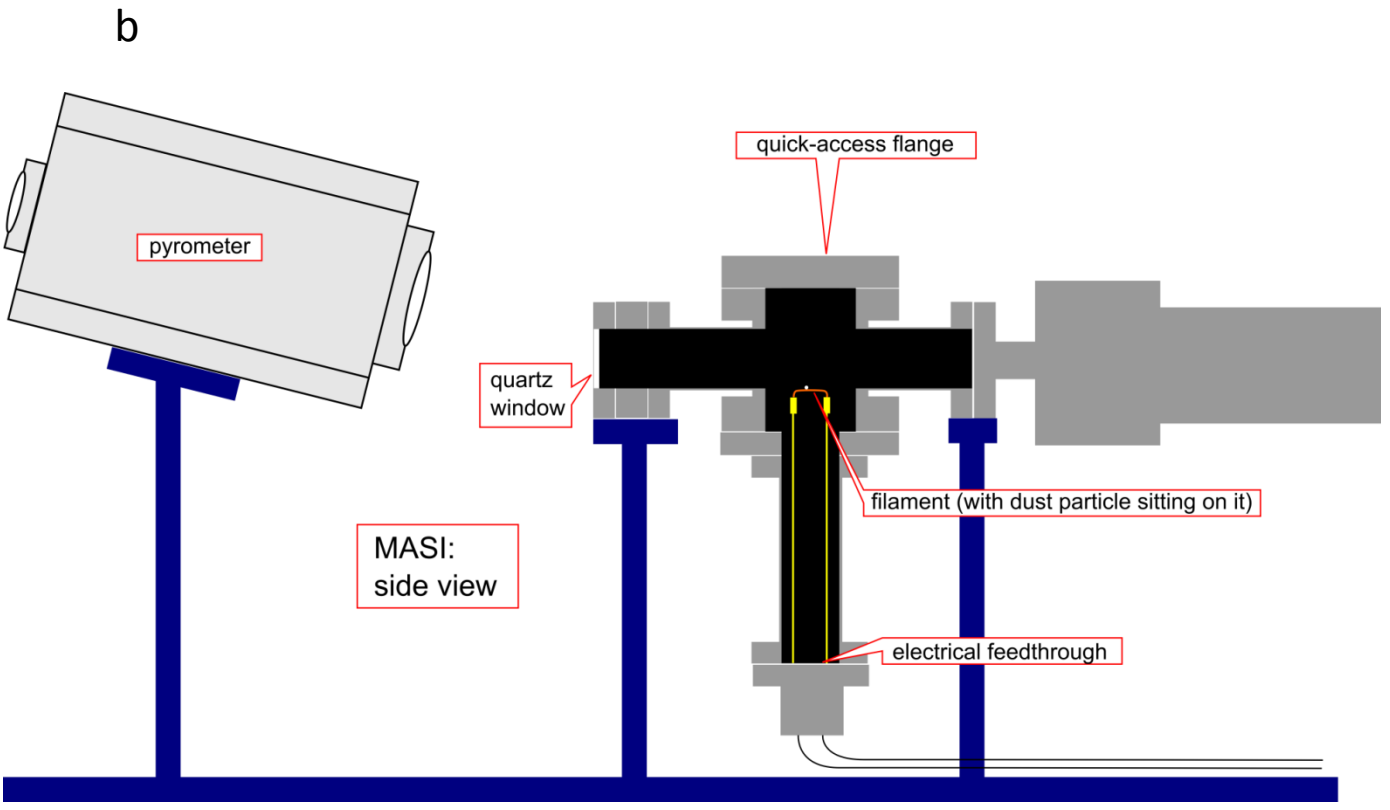
b
pyrometer
quick-access flange
quartz
window
filament (with dust particle sitting on it)
MASI:
side view
electrical feedthrough


a
<38
38-106
106-150
150-250
250-355
>355

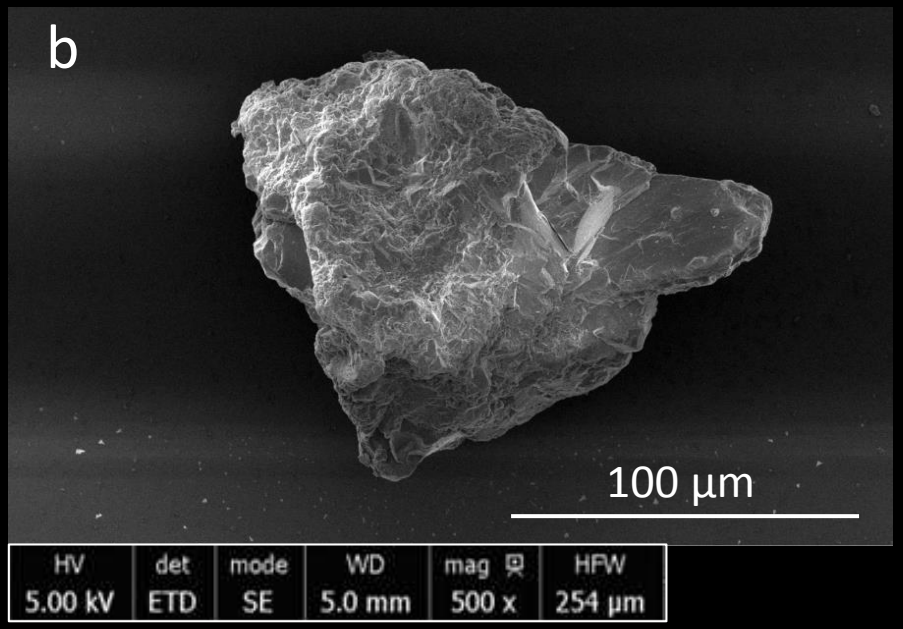
b
100 µm
HV
5.00 kV
det
ETD
mode
SE
WD
5.0 mm
mag
500 x
HFW
254 µm

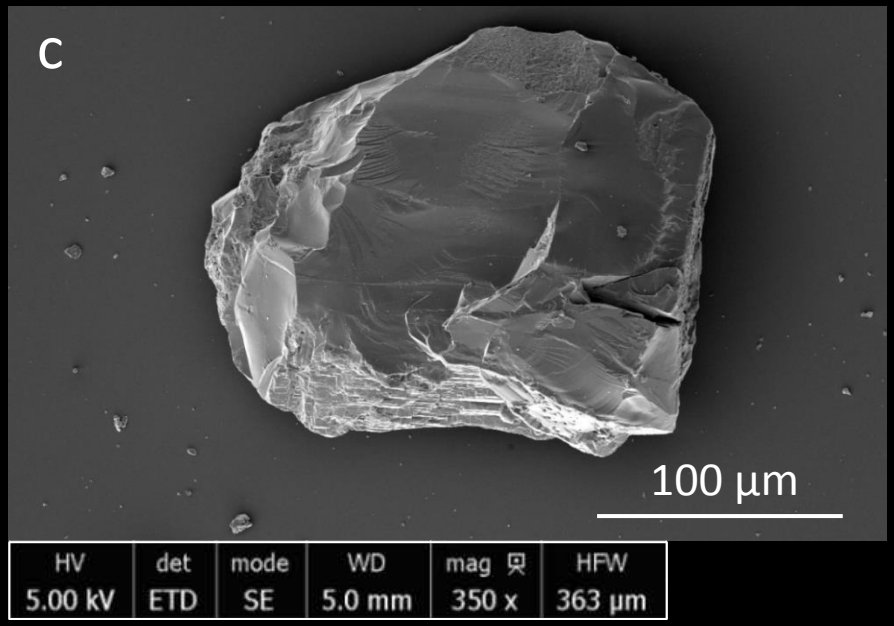
c
100 µm
HV
5.00 kV
det
ETD
mode
SE
WD
5.0 mm
mag
350 x
HFW
363 µm

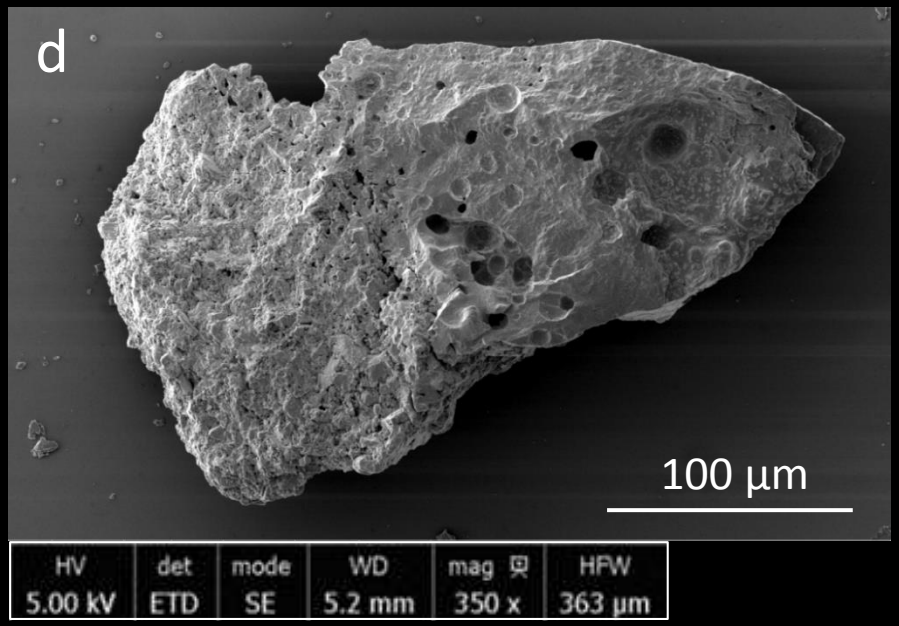
d
100 µm
HV
5.00 kV
det
ETD
mode
SE
WD
5.2 mm
mag
350 x
HFW
363 µm

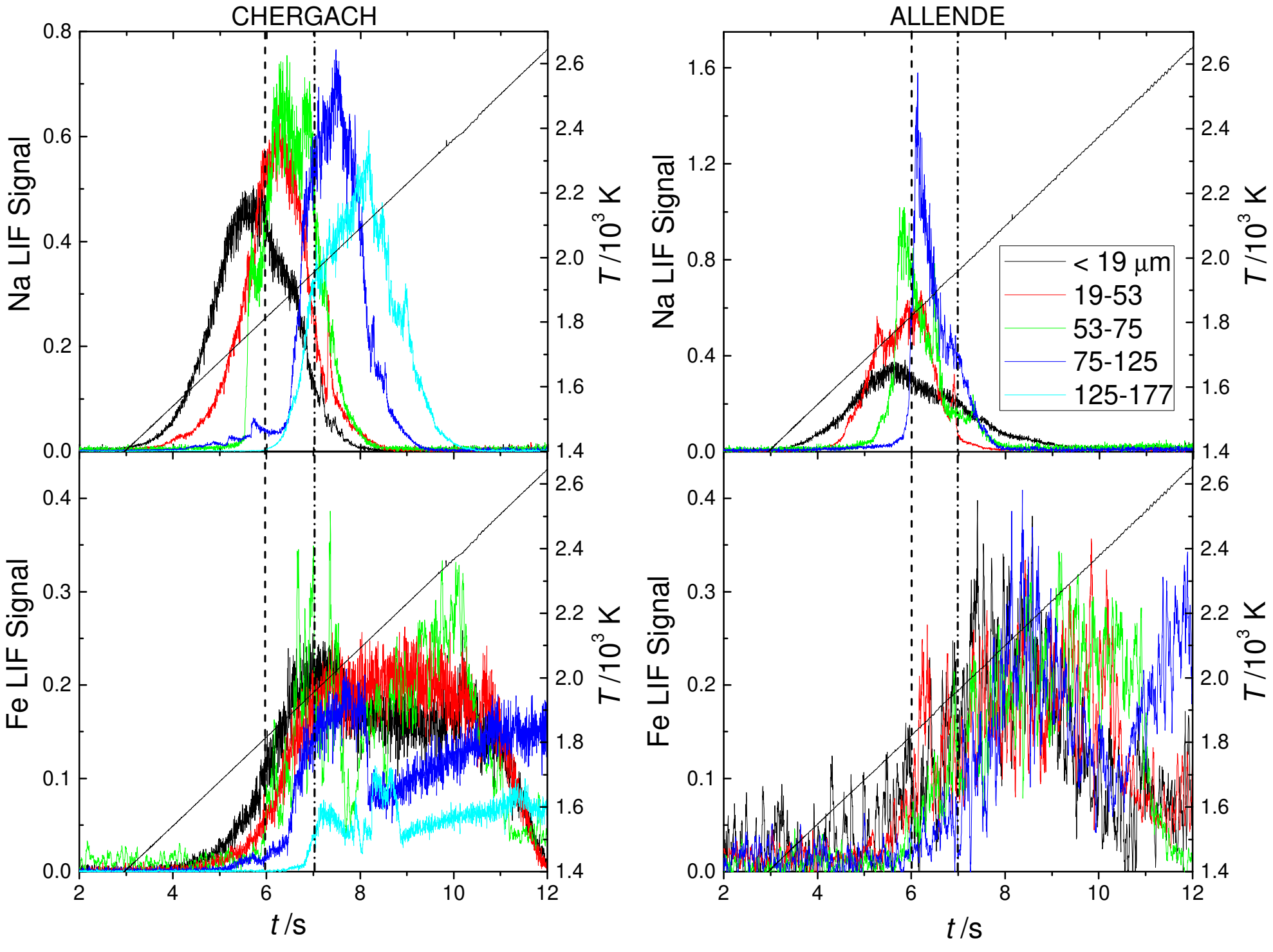
CHERGACH
ALLENDE
Na LIF Signal
Fe LIF Signal
T /10^3 K
t /s
< 19 μm
19-53
53-75
75-125
125-177

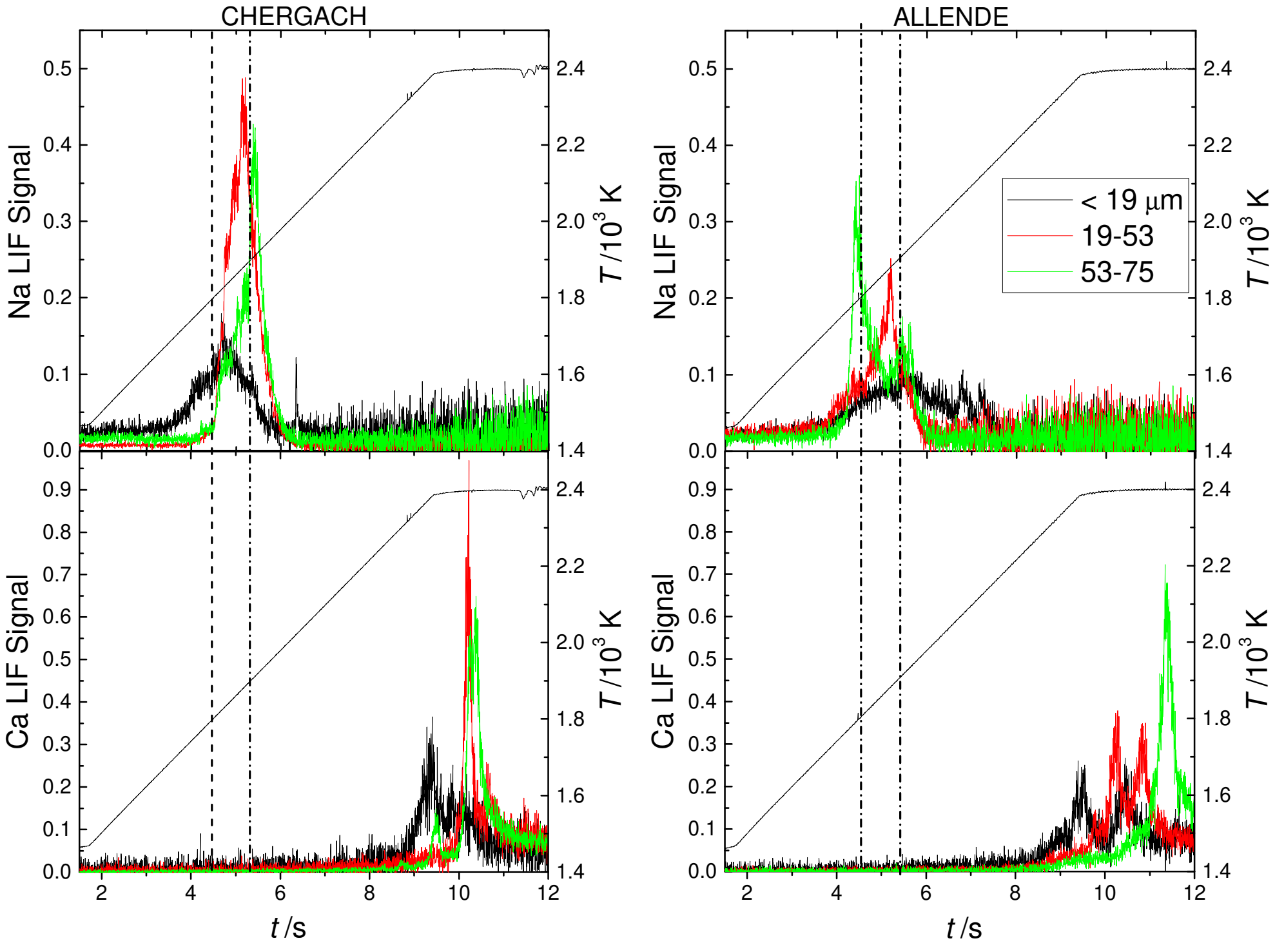
CHERGACH
ALLENDE
Na LIF Signal
Ca LIF Signal
T /10^3 K
t /s
< 19 μm
19-53
53-75

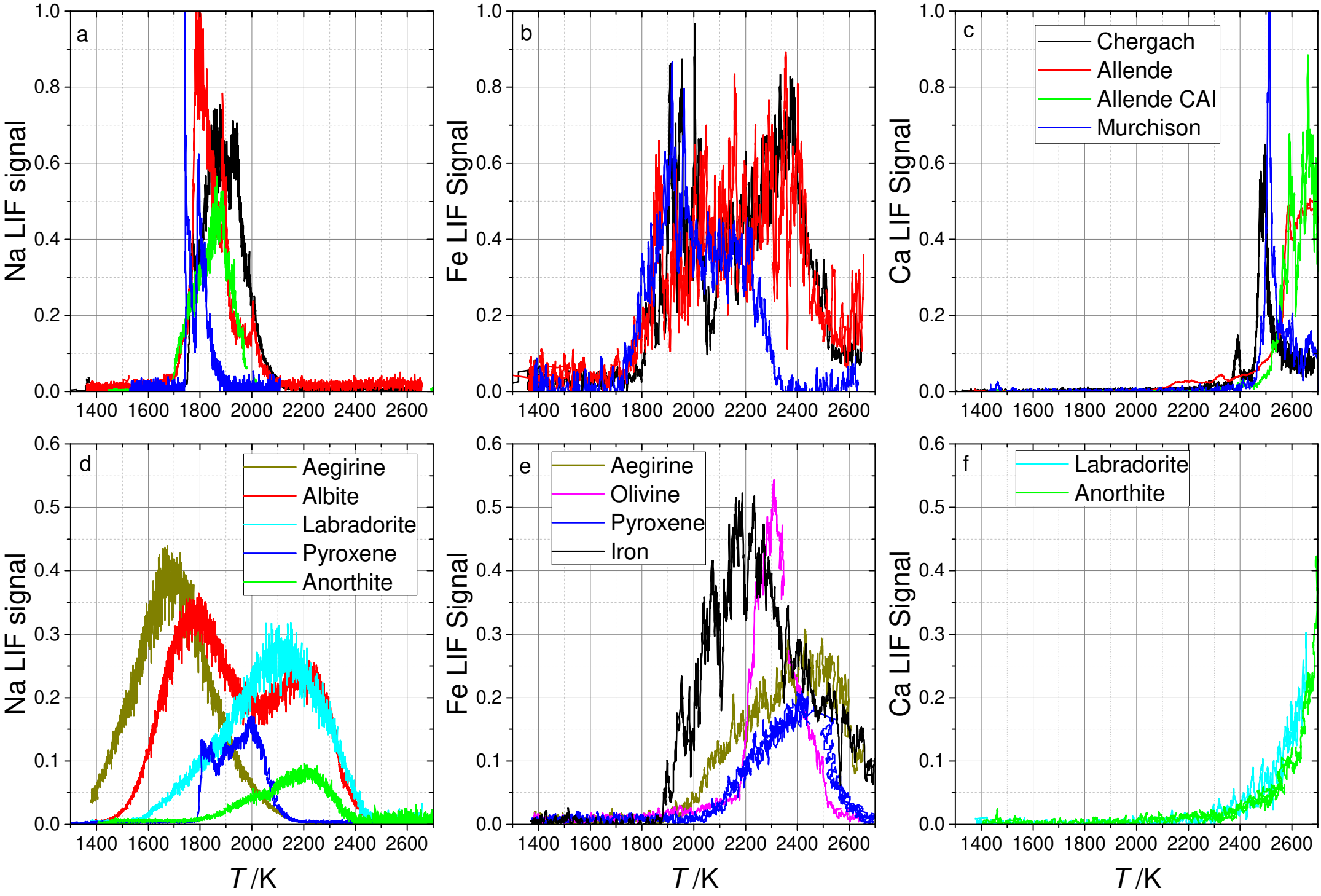
a
b
c
d
e
f
Na LIF signal
Fe LIF Signal
Ca LIF Signal
T /K
Chergach
Allende
Allende CAI
Murchison
Aegirine
Albite
Labradorite
Pyroxene
Anorthite
Olivine
Iron

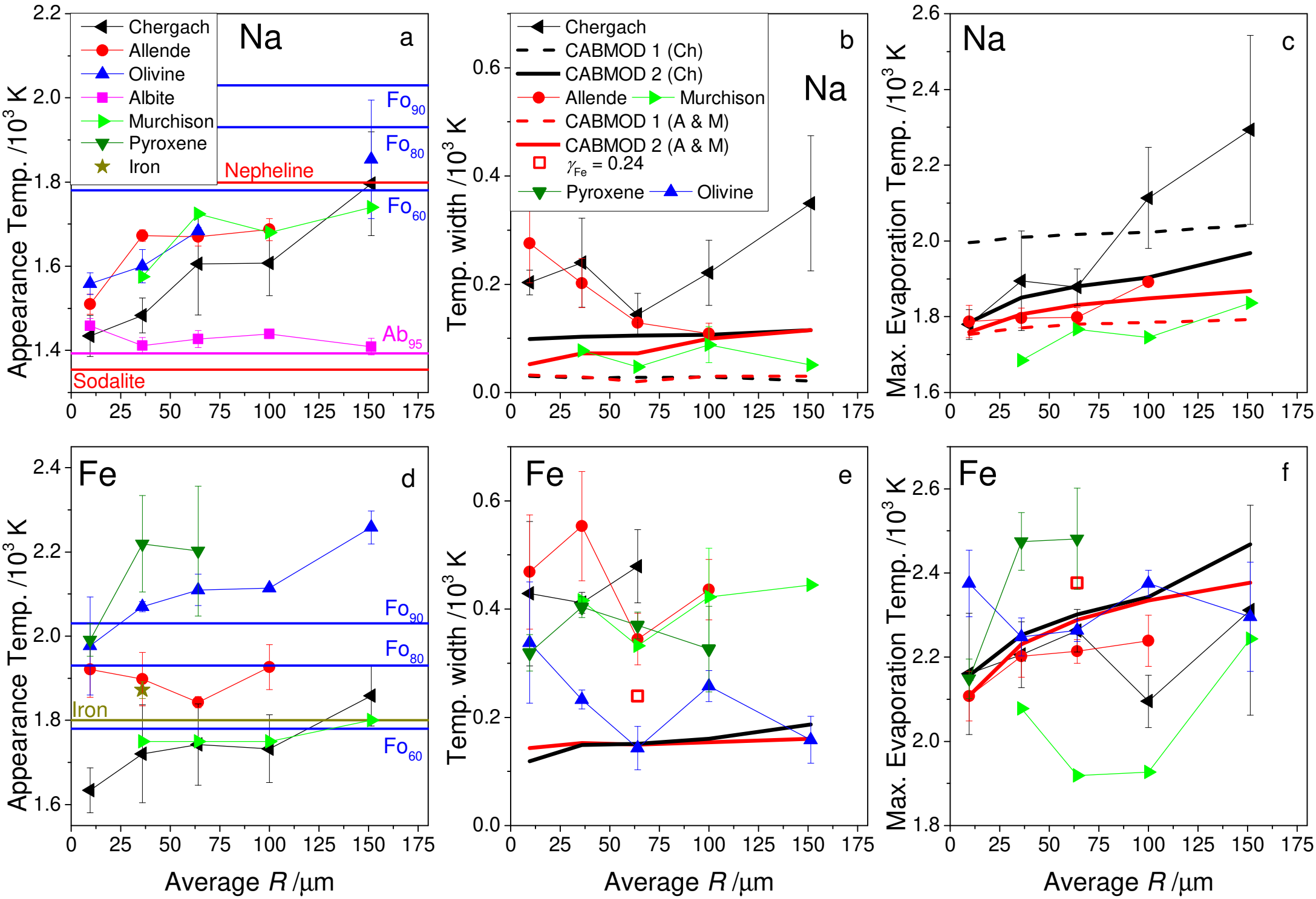
Na
a
Chergach
Allende
Olivine
Albite
Murchison
Pyroxene
Iron
Fo90
Fo80
Nepheline
Fo60
Ab95
Sodalite
Appearance Temp. /10^3 K
b
Na
CABMOD 1 (Ch)
CABMOD 2 (Ch)
CABMOD 1 (A & M)
CABMOD 2 (A & M)
γFe = 0.24
Temp. width /10^3 K
c
Max. Evaporation Temp. /10^3 K
Fe
d
e
f
Average R /μm

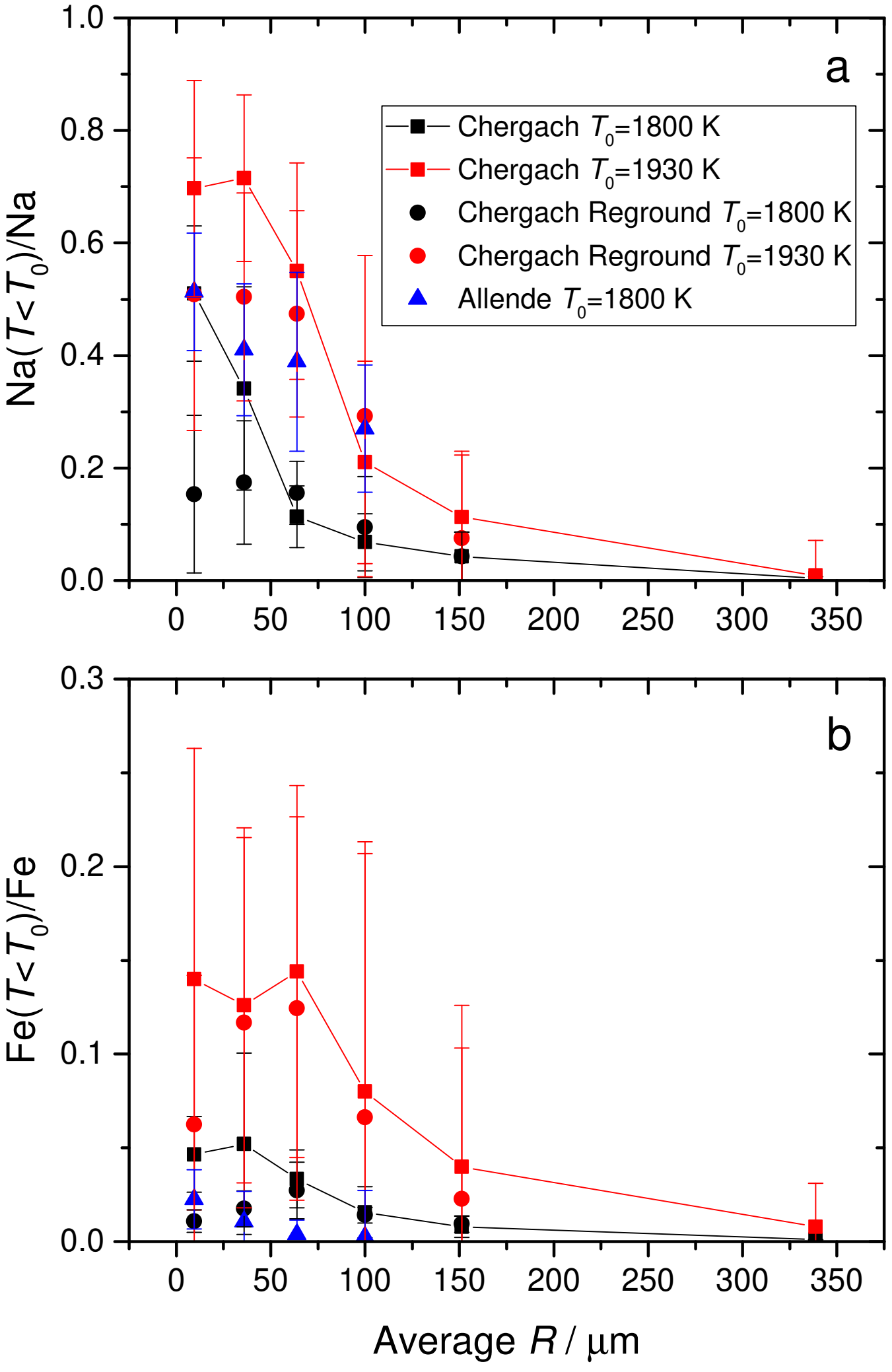
a
b
Chergach T_0=1800 K
Chergach T_0=1930 K
Chergach Reground T_0=1800 K
Chergach Reground T_0=1930 K
Allende T_0=1800 K
Na($T<T_0$)/Na
Fe($T<T_0$)/Fe
Average R / μm
0.0
0.2
0.4
0.6
0.8
1.0
0.1
0.3
0
50
100
150
200
250
300
350

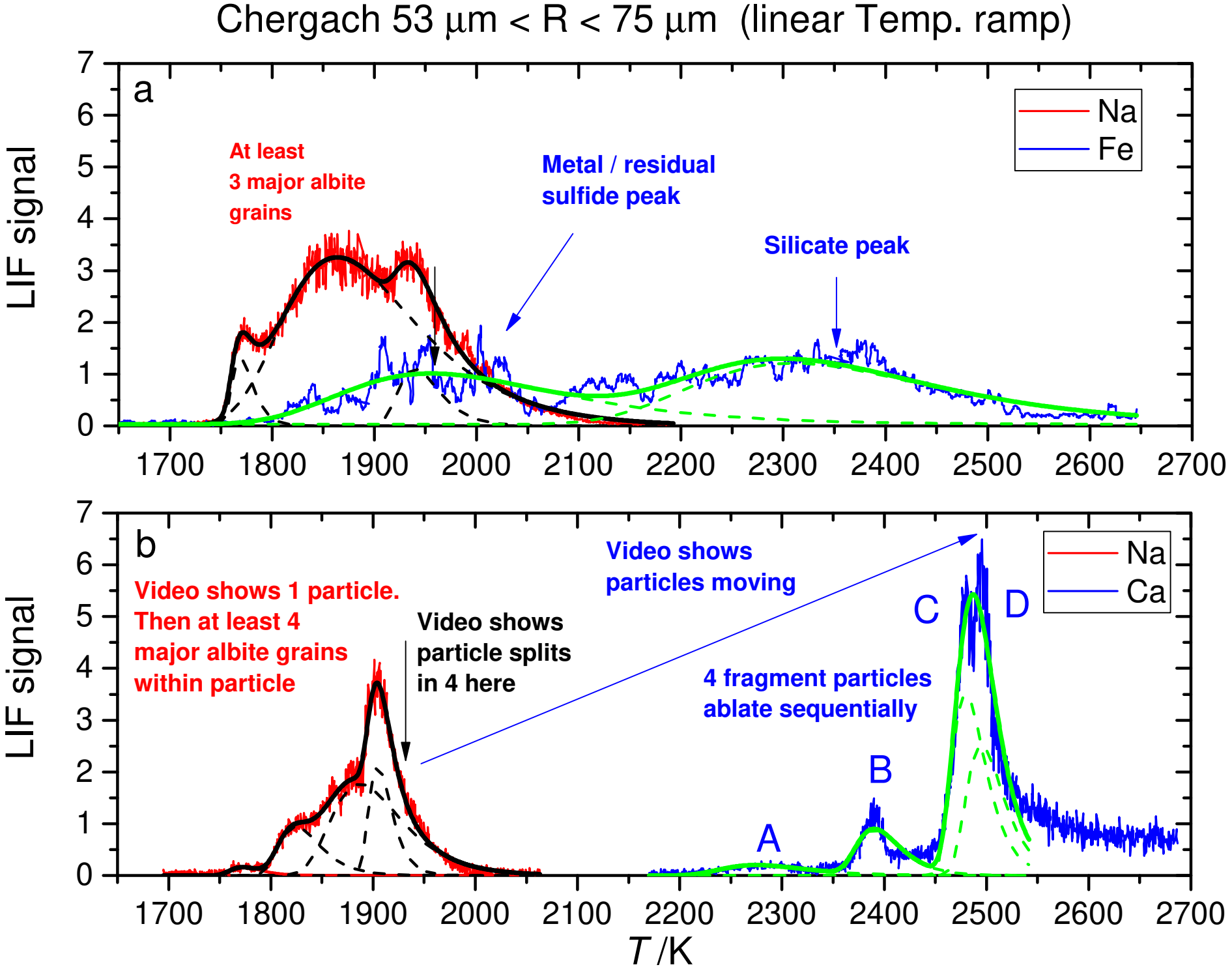
Chergach 53 μm < R < 75 μm (linear Temp. ramp)
a
LIF signal
Na
Fe
At least
3 major albite
grains
Metal / residual
sulfide peak
Silicate peak
b
Video shows 1 particle.
Then at least 4
major albite grains
within particle
Video shows
particle splits
in 4 here
Video shows
particles moving
4 fragment particles
ablate sequentially
Na
Ca
A
B
C
D
T /K

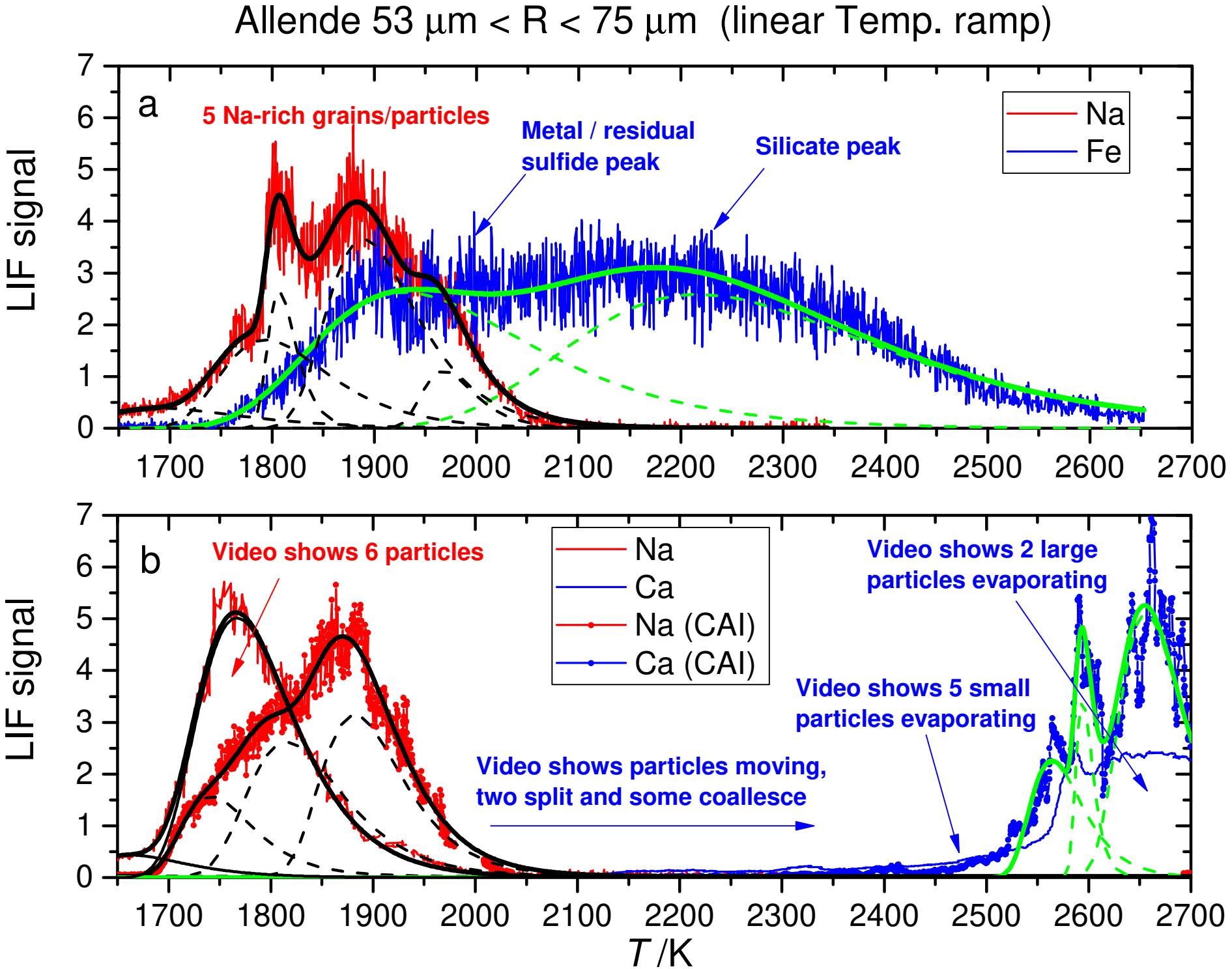
Allende 53 μm < R < 75 μm (linear Temp. ramp)
a
5 Na-rich grains/particles
Metal / residual sulfide peak
Silicate peak
Na
Fe
LIF signal
b
Video shows 6 particles
Na
Ca
Na (CAI)
Ca (CAI)
Video shows 2 large particles evaporating
Video shows 5 small particles evaporating
Video shows particles moving, two split and some coallesce
LIF signal
T /K

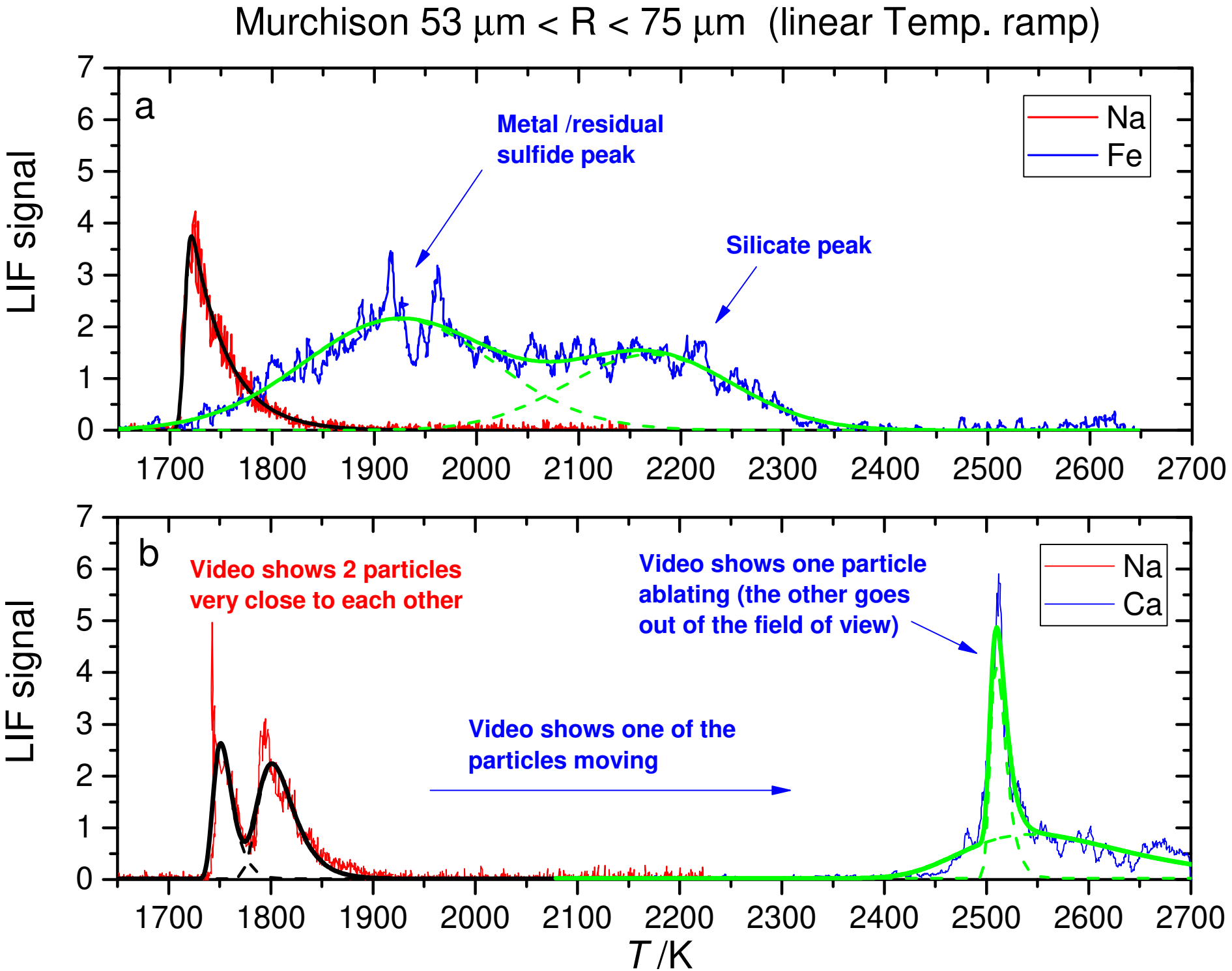
Murchison 53 µm < R < 75 µm (linear Temp. ramp)
a
Metal /residual sulfide peak
Silicate peak
Na
Fe
LIF signal
b
Video shows 2 particles very close to each other
Video shows one particle ablating (the other goes out of the field of view)
Video shows one of the particles moving
Na
Ca
LIF signal
T /K

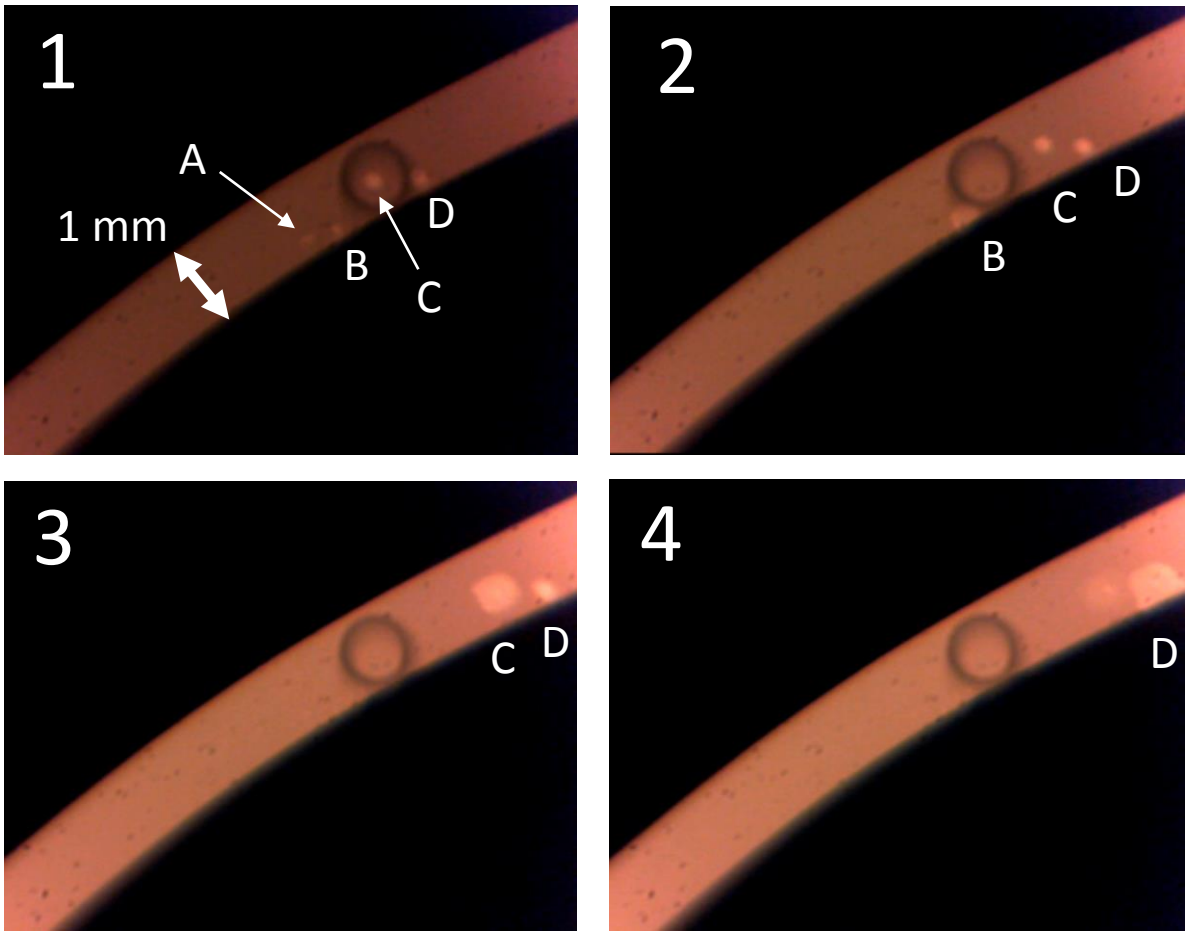
1
A
1 mm
B
C
D
2
B
C
D
3
C
D
4
D

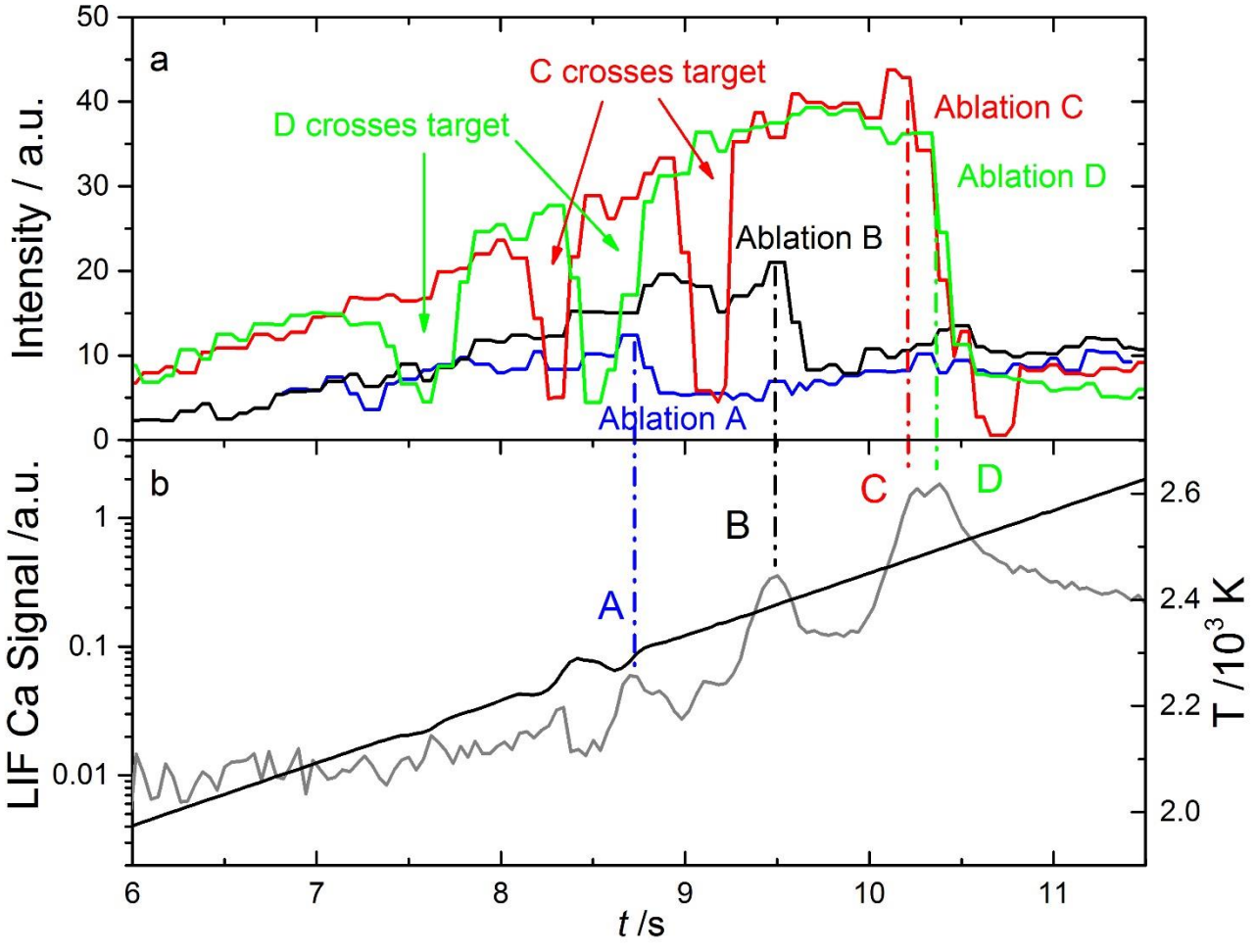
a
Intensity / a.u.
D crosses target
C crosses target
Ablation C
Ablation D
Ablation B
Ablation A
b
LIF Ca Signal /a.u.
T /10^3 K
A
B
C
D
t /s

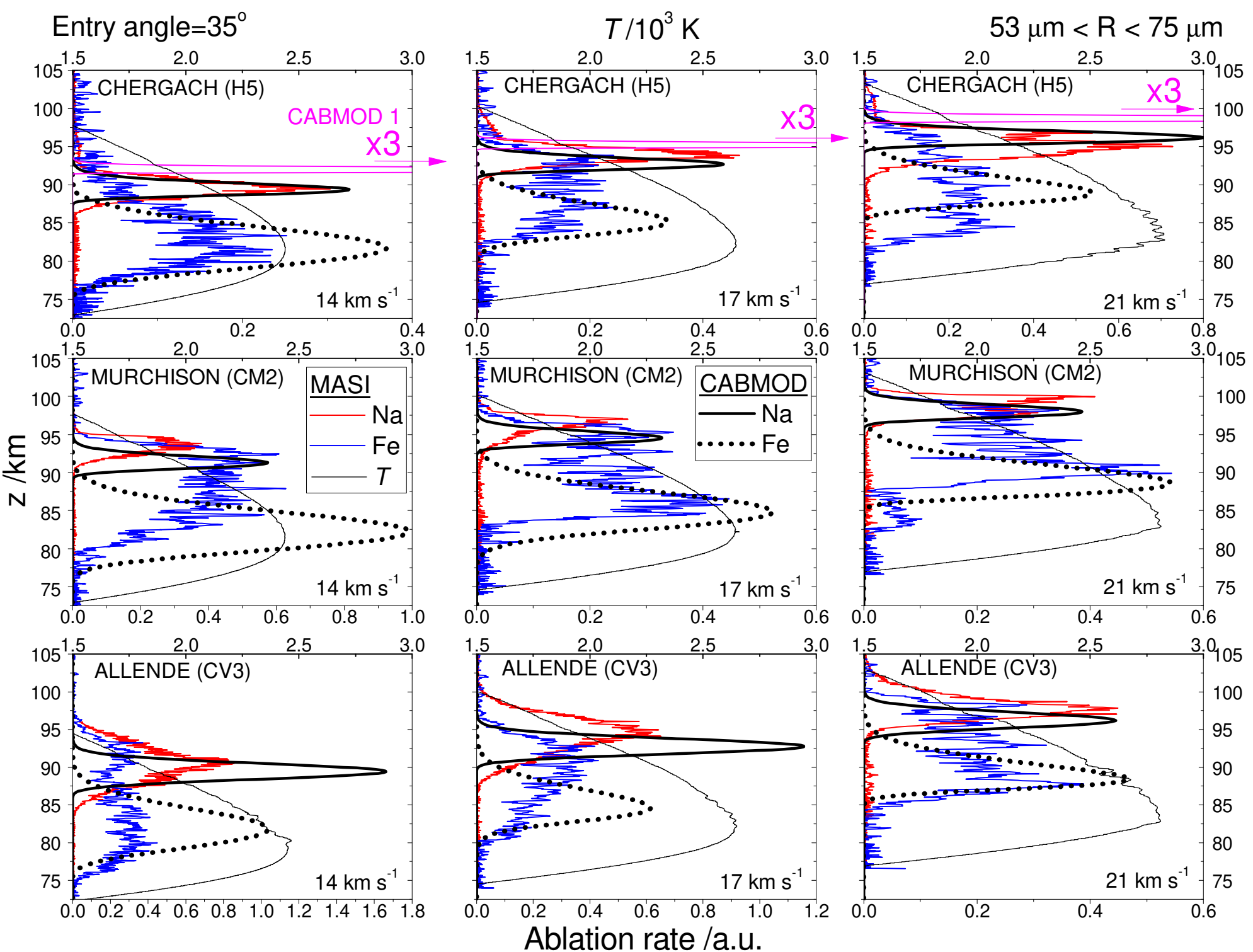
Entry angle=35°
T /10^3 K
53 μm < R < 75 μm
CHERGACH (H5)
CABMOD 1
x3
14 km s^-1
17 km s^-1
21 km s^-1
MURCHISON (CM2)
ALLENDE (CV3)
MASI
Na
Fe
T
CABMOD
z /km
Ablation rate /a.u.

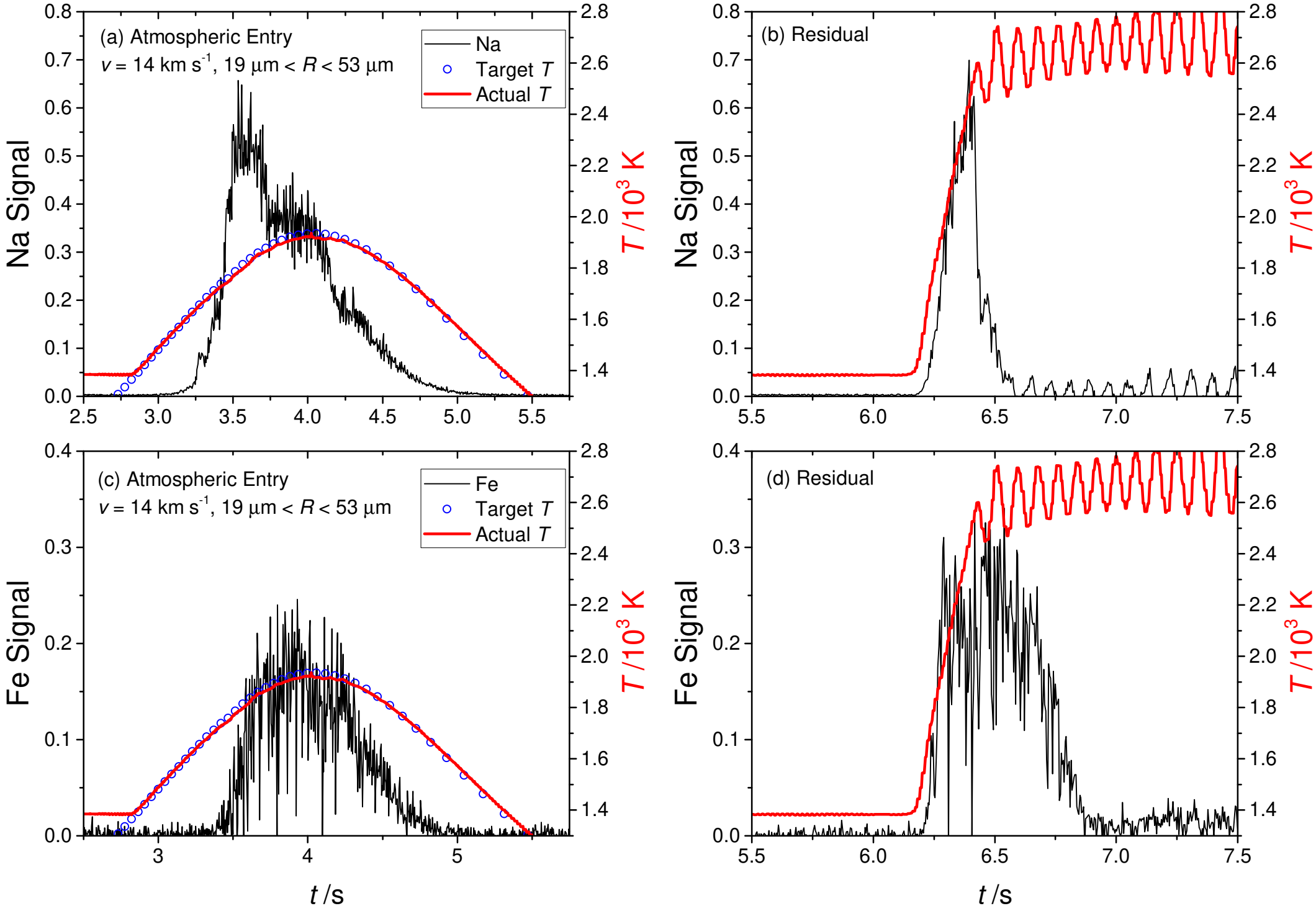
(a) Atmospheric Entry
v = 14 km s-1, 19 μm < R < 53 μm
Na
Target T
Actual T
Na Signal
T /10^3 K
(b) Residual
(c) Atmospheric Entry
v = 14 km s-1, 19 μm < R < 53 μm
Fe
Target T
Actual T
Fe Signal
T /10^3 K
(d) Residual
t /s
t /s

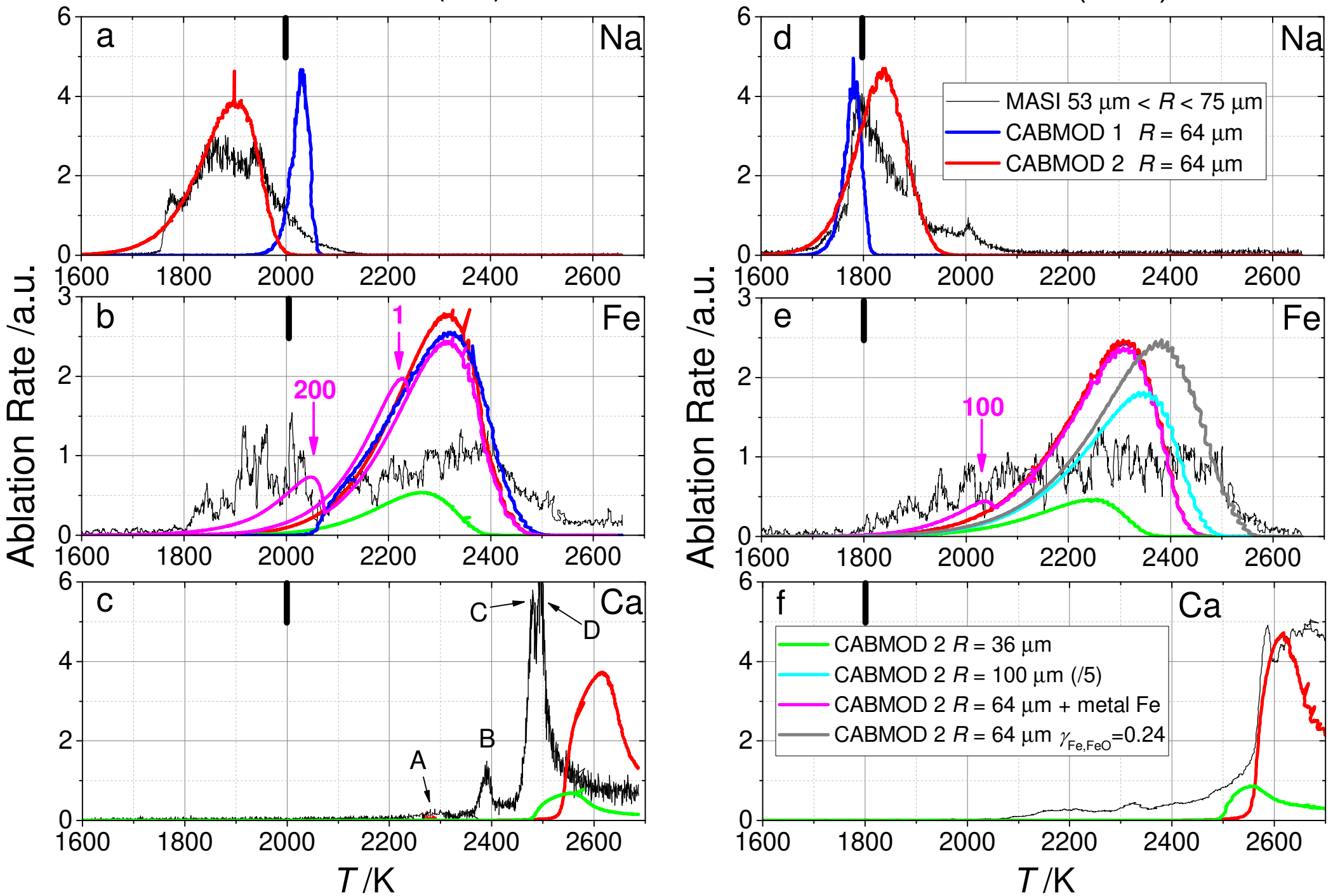
CHERGACH (H5)
ALLENDE (CV3)
a
Na
b
Fe
c
Ca
d
e
f
1
200
100
A
B
C
D
MASI 53 μm < R < 75 μm
CABMOD 1 R = 64 μm
CABMOD 2 R = 64 μm
CABMOD 2 R = 36 μm
CABMOD 2 R = 100 μm (/5)
CABMOD 2 R = 64 μm + metal Fe
CABMOD 2 R = 64 μm γFe,FeO=0.24
Ablation Rate /a.u.
T /K

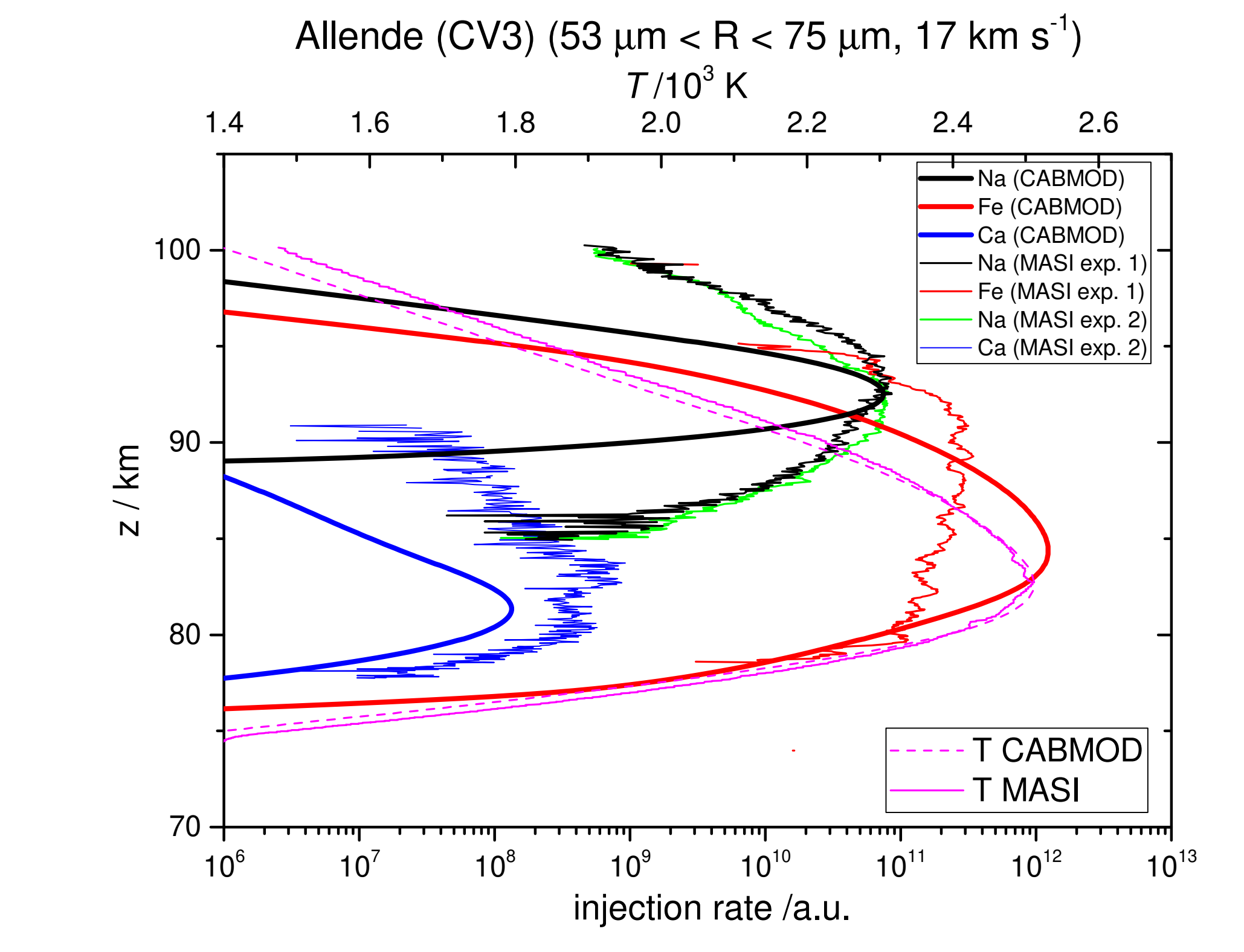
Allende (CV3) (53 µm < R < 75 µm, 17 km s-1)
T /10^3 K
1.4
1.6
1.8
2.0
2.2
2.4
2.6
Na (CABMOD)
Fe (CABMOD)
Ca (CABMOD)
Na (MASI exp. 1)
Fe (MASI exp. 1)
Na (MASI exp. 2)
Ca (MASI exp. 2)
T CABMOD
T MASI
z / km
100
90
80
70
10^6
10^7
10^8
10^9
10^10
10^11
10^12
10^13
injection rate /a.u.

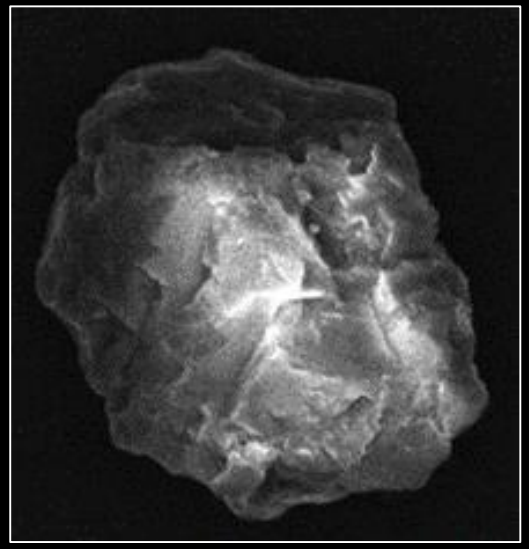

Micrograph

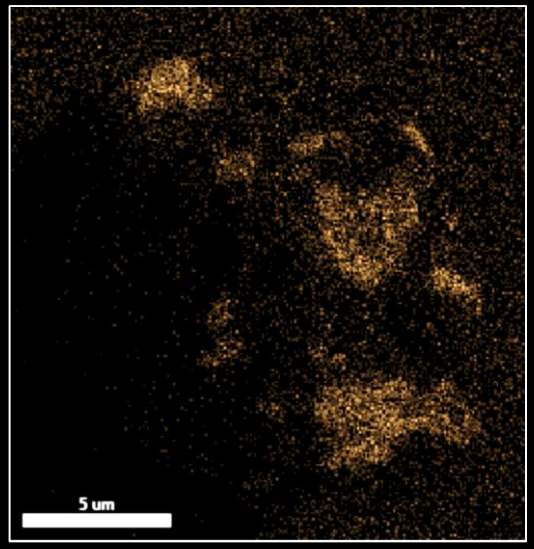

Na

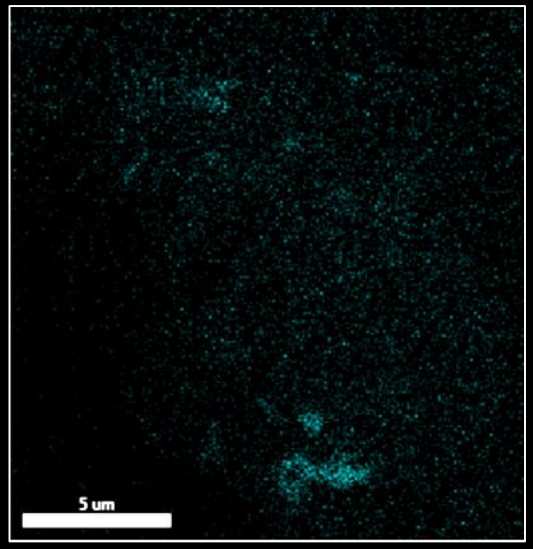

Ca

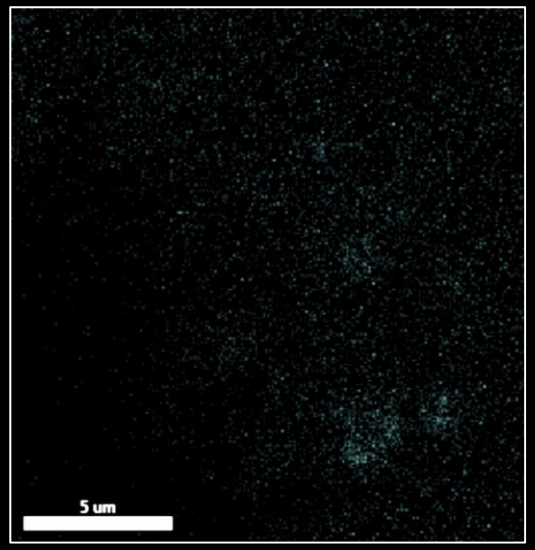

K

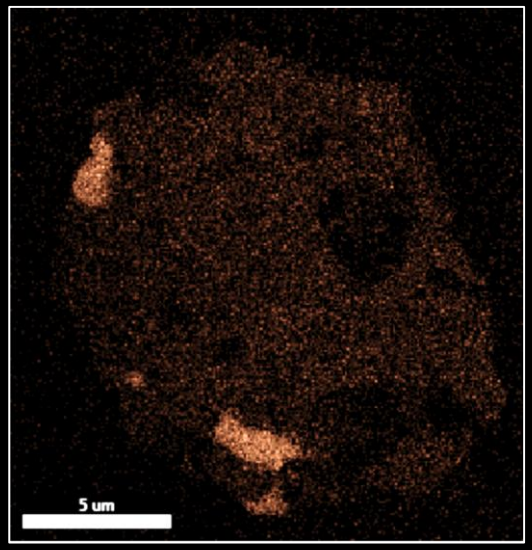

Fe

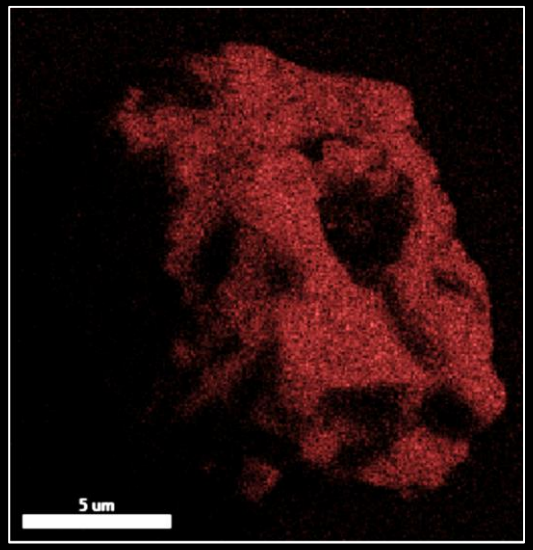

Mg

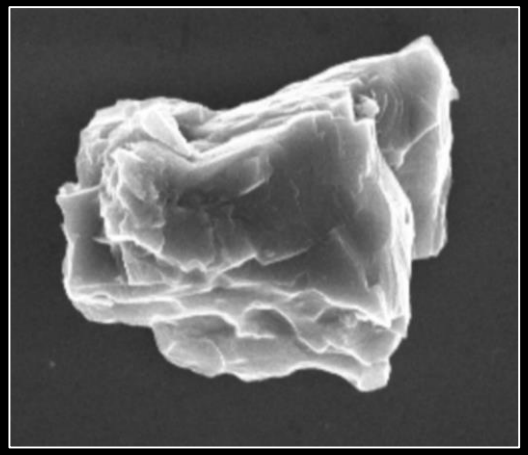

Micrograph

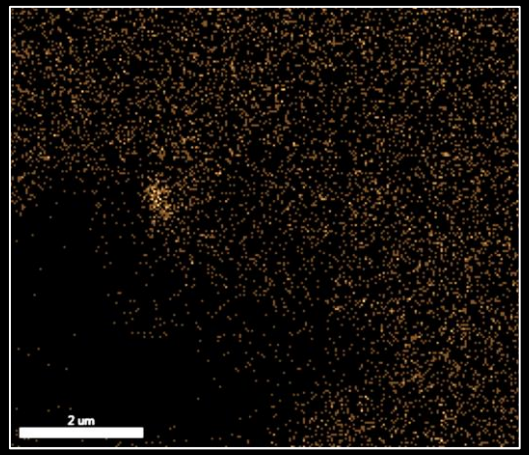

Na

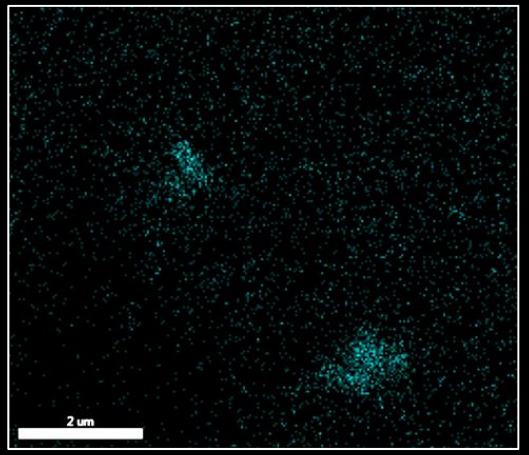

Ca

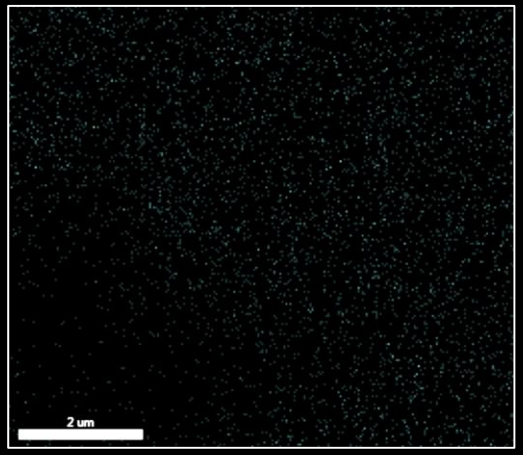

K

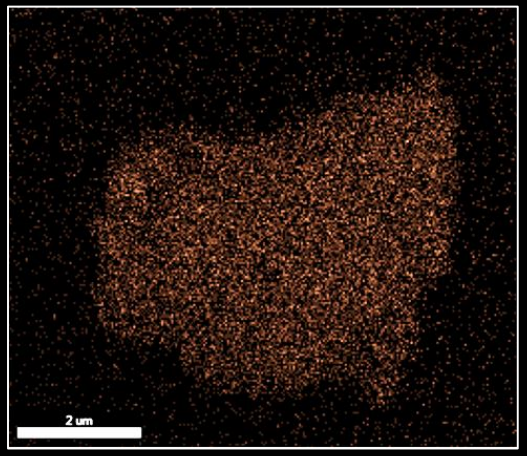

Fe

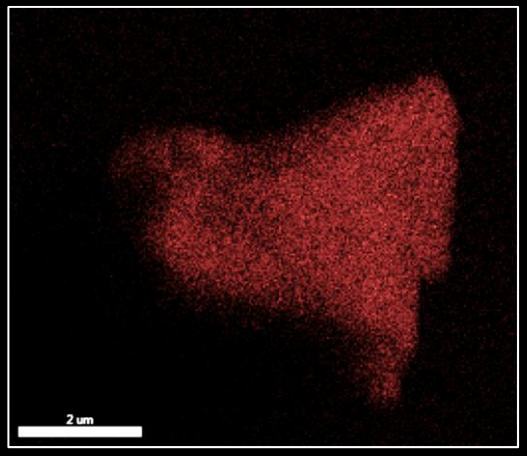

Mg

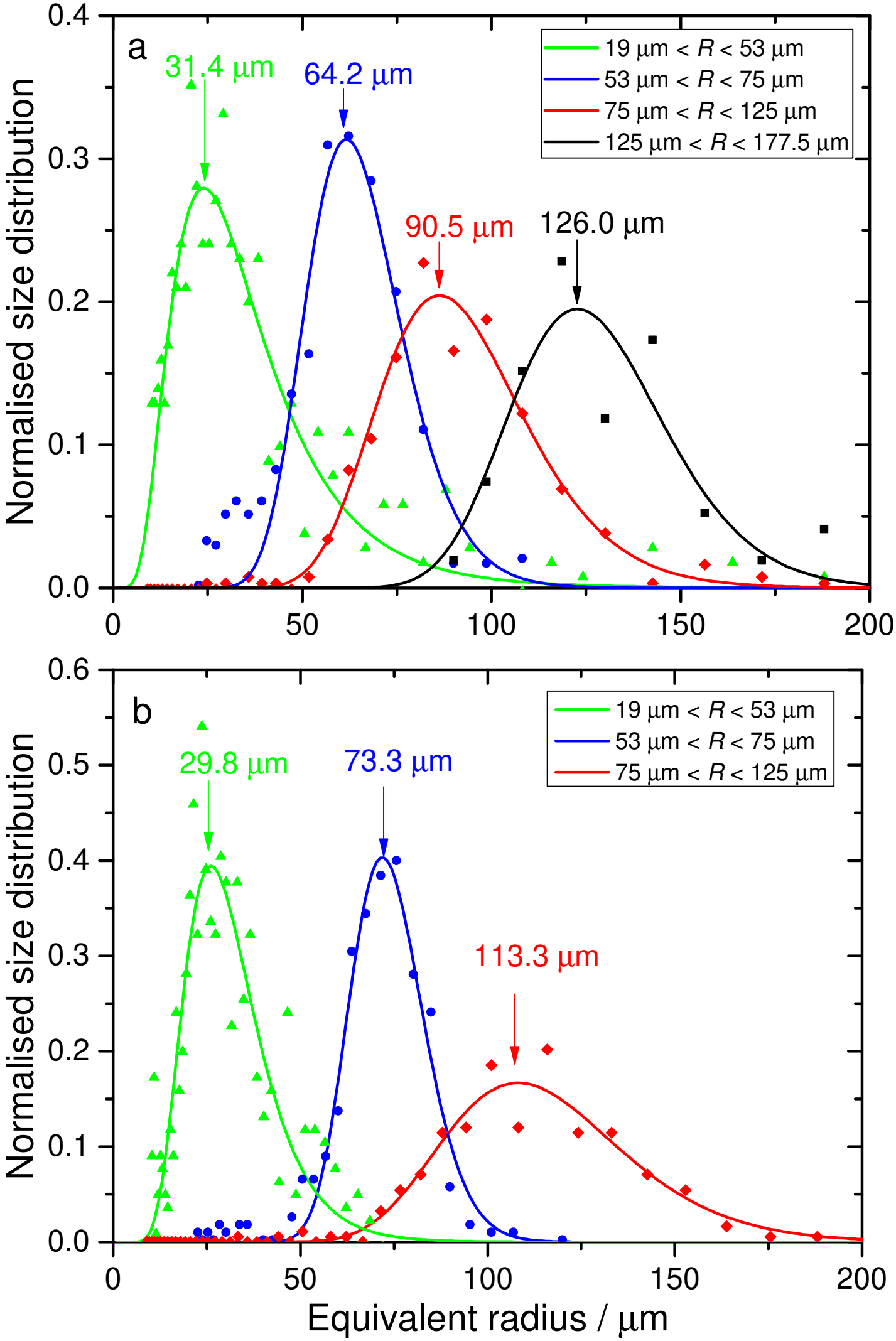
a
31.4 µm
64.2 µm
90.5 µm
126.0 µm
19 µm < R < 53 µm
53 µm < R < 75 µm
75 µm < R < 125 µm
125 µm < R < 177.5 µm
Normalised size distribution
0.0
0.1
0.2
0.3
0.4
0
50
100
150
200
b
29.8 µm
73.3 µm
113.3 µm
19 µm < R < 53 µm
53 µm < R < 75 µm
75 µm < R < 125 µm
Normalised size distribution
0.0
0.1
0.2
0.3
0.4
0.5
0.6
0
50
100
150
200
Equivalent radius / µm